

Linköping University | Department of Management and Engineering

Master's thesis, 30 credits | Master's programme

Spring 2020

ISRN: LIU-IEI-TEK-A--20/03913--SE

# Material parameter identification of a thermo-plastic using full-field calibration

**Nikhil Prabhu**

Supervisor: Joakim Holmberg

Examiner: Stefan Lindström

Industrial supervisor: Björn Stoltz

# Abstract

Finite element simulation of thermoplastic components is gaining importance as the companies aim to avoid overdesign of the components. Cost of the component can be minimized by using an adequate amount of material for its application. Life of the component, in a particular application, can be predicted as early as during its design phase with the help of computer simulations. To achieve reliable simulation results, an accurate material model which can predict the material behaviour is vital. Most material models consist of a number of material parameters that needs to be fed into them. These material parameters can be identified with the inputs from physical tests. The accuracy of the data extracted from the physical tests, however, remains the base for the aforementioned process.

The report deals with the implementation of optical measurement technique such as Digital Image Correlation (DIC) in contrast with the conventional extensometers. A tensile test is conducted on a glass fibre reinforced thermoplastic specimen, according to ISO 527-2/1A, to extract the experimental data with the help of DIC technique. The material behavior is reproduced within a finite element analysis software package LS-DYNA, with the combination of elastoplastic model called \*MAT\_024 and stress state dependent damage and failure model called GISSMO. The tensile test is performed under quasi-static condition to rule out the strain rate dependency of the thermoplastic material. The mesh sensitivity of the damage model is taken into account with the element size regularization.

The thesis concerns setting up a routine for material parameter identification of thermoplastics by full-field calibration (FFC) approach. Also, comparison of the strain field in the specimen, obtained through the newly set up routine against the regular non-FFC i.e. extensometer measurement routine. The major objective being, through the comparisons, a qualitative assessment of the two routines in terms of calibration time vs. gain in simulation accuracy. Material models obtained through both the routines are implemented in three-point and four-point bending simulations. The predicted material behaviors are evaluated against experimental tests.

# Acknowledgements

The master's thesis was carried out at IKEA Components AB in Älmhult in cooperation with the Division of Solid Mechanics at Linköping University. The experiments were conducted at IKEA Test Lab in Älmhult. The thesis was started on 27 January 2020 and presented at the University on 25 September 2020.

I would like to thank IKEA Components AB for giving me this opportunity to carry out the thesis and Björn Stoltz, who was the supervisor at the company, for his constant support and valuable insights during the thesis. I would like to express my gratitude to Joakim Holmberg, who was the thesis supervisor at Linköping University. I would also want to thank David Aspenberg and Mikael Schill at DYNAmore Nordic, Linköping for their guidance, supervision and software training during the thesis. My special thanks to Marko Kokkonen for his assistance during the experiments at IKEA Test Lab.

Linköping, September 2020  
Nikhil Prabhu

# Contents

<b>Abstract.....</b>	<b>ii</b>
<b>Acknowledgements .....</b>	<b>iii</b>
<b>1. Introduction .....</b>	<b>1</b>
1.1    About IKEA.....	1
1.2    Background.....	1
1.3    Objectives.....	2
<b>2. The Digital Image Correlation Technique .....</b>	<b>3</b>
2.1    Initial setup.....	3
2.2    Computation of strain: Theory .....	4
2.3    Computation of strain: Procedure.....	5
<b>3. Theory.....</b>	<b>6</b>
3.1    Material Models in LS-DYNA .....	6
3.1.1    MAT_PIECEWISE_LINEAR_PLASTICITY .....	6
3.1.2    MAT_ADD_EROSION.....	8
3.2    Optimization.....	11
3.2.1    Response Surface Methodology .....	11
3.2.2    Mean Square Error .....	13
3.2.3    Dynamic Time Warping .....	14
3.3    Three-point bending.....	14
3.4    Four-point bending.....	16
<b>4. Method.....</b>	<b>17</b>
4.1    Material parameter identification.....	17
4.2    Material testing .....	17
4.3    Modelling in LS-PrePost.....	20
4.4    Optimization set up in LS-OPT .....	23
4.4.1    Introduction.....	23
4.4.2    Regular routine .....	24
4.4.3    FFC routine .....	25
4.5    Element size regularization.....	25
4.6    Comparisons .....	26
<b>5. Results.....</b>	<b>27</b>

5.1	Regular vs. FFC routine .....	27
5.2	Comparisons with different extensometer gauge lengths .....	29
5.3	Element size regularization.....	30
5.4	Three-point bending.....	31
5.5	Four-point bending.....	31
<b>6.</b>	<b>Discussion.....</b>	<b>34</b>
<b>7.</b>	<b>Conclusion and future work .....</b>	<b>36</b>
7.1	Conclusions.....	36
7.2	Future work.....	36
	<b>References .....</b>	<b>37</b>
	<b>Appendix 1: Example: DTW .....</b>	<b>39</b>
	<b>Appendix 2: Generic specimen from bending tests .....</b>	<b>41</b>
	<b>Appendix 3: A short study on PA6 Material .....</b>	<b>42</b>

# 1. Introduction

## 1.1 About IKEA

IKEA was founded in Älmhult, Sweden by Ingvar Kamprad in 1943. Since then, it has gone from being a tiny mail-order company, to becoming one of the most well-known home furnishing brands in the world. With a business idea, “to offer a wide range of well-designed, functional home furnishing products at prices so low that as many people as possible will be able to afford them”, IKEA has always been striving to do everything a little better, a little simpler, more efficiently and always cost-effectively.

In 1985 Ingvar Kamprad and the IKEA board realised that suppliers used same fittings on multiple furniture and therefore decided to start IKEA’s first subsidiary: MODUL Service, that later on in 2007 changed name to IKEA Components. IKEA Components, with an assignment to develop, source, pack and supply components in areas where it benefits IKEA and its customers, focusses on creating price advantage through business development and economy of scale. Currently, with about 1500 employees, IKEA Components’ offices are based in Sweden, Slovakia and China.

## 1.2 Background

Because of large scale production of the components, every small detail will have an impact on the final price. Keeping that in mind, IKEA Components aims to avoid overdesign of the components. An important development strategy within IKEA is to create a product which enables easy assembly for the end customer. Hence, a more advanced fitting with aesthetics such as delightful colour and shape, at low cost is desired. Thereby the demand for thermoplastic materials in the current application is increasing. In its expedition of being climate positive, IKEA focusses on replacing fossil fuel-based thermoplastics with bio-based thermoplastics. The new materials that are intended to be used need a calibration of parameters that are present in material models in the finite element software packages. For accurate simulation of the material behaviour, the material parameters are to be identified through a calibration against an accurate experimental data. “The goal of material parameter identification is to characterize the constitutive behaviour using experimental results in combination with structural modelling of test samples” (Stander, Witowski et al. 2018).

Tensile testing is a commonly used method for material parameter identification where a test specimen is subjected to a force and measured for deformation. As of now at IKEA Test Lab, the Digital Image Correlation (DIC) system is used to measure the deformation with the help of homologous point tracing during the material testing. Meaning that the DIC system would only act as a virtual extensometer which calculates deformations, across a gauge length, between two points. The extracted global data would then undergo a regular routine for calibration and the material parameters were identified. However, the capabilities of the DIC system were not fully utilized. Also, during the complex phenomena like strain localization and failure, the strain field in the test specimen will be non-uniform. The impact of reference length in the computation of strain across

a localization region is clearly depicted in (Ilg, Haufe et al. 2018). Therefore, there is a need for extracting data not only as global quantities, but also as local (in the region around localization) quantities to accurately model the material behaviour.

### 1.3 Objectives

The test samples used in this thesis are made up of a glass fibre reinforced thermoplastic material. A standard uniaxial tensile test will be conducted on five test samples and the DIC system will be used to extract both local and global physical quantities. The data extracted from the most generic test specimen will be considered as the input test data. The choice of the most generic test sample will be carried out according to IKEA's in-house scripts\*. A new routine will be set up for identifying material parameters by using the force vs. full-field strain data as target data in LS-OPT. Material parameter identification will also be carried out by using the force vs. global strain data by adopting the regular routine†. A comparison among the strain field in the specimens obtained from the experiment, by calibration through the regular routine and the newly set up routine is to be made. Through the comparisons, a qualitative assessment of the two routines in terms of calibration time vs. gain in simulation accuracy will be carried out.

The material models that are to be used in LS-DYNA consist of a combination of \*MAT\_024 and \*MAT\_ADD\_EROSION. The optimization of material parameters will be carried out in LS-OPT with an objective to minimize the distance functional between the experimental data and the computed results. Similarity measures such as Mean Square Error and normalised Dynamic Time Warping will be adopted based on the nature of responses that are to be matched.

A similar material testing procedure, without extraction of full-field data, will be carried out for three-point and four-point bending tests. The material models, obtained from calibration against the tensile test, will be used to simulate the bending tests in the software. Comparisons among the experimental and simulation results are to be made with comments on further possible enhancements in the routines. To determine the credibility of the simulation models, the three-point and four-point bending models will be validated against analytical solutions obtained in the elastic regime.

---

\* The Script imports material parameters and their corresponding weights, that are chosen by the operator, and determines the most generic test sample based on the mean value among the test samples.

† Regular routine, in this thesis, refers to the process of calibration against the force vs. true strain data extracted by the 75 mm gauge length virtual extensometer.

## 2. The Digital Image Correlation Technique

### 2.1 Initial setup

The DIC software, ARAMIS Professional by GOM GmbH, calculates the strain in the test specimen with the help of stochastic image information present on its surface. To obtain this random pattern on the surface, the test specimen is painted white to have a clear bright background and then sprayed randomly with graphite coating. A specimen with a dark stochastic speckle pattern against a bright white background on its surface is presented in [Figure 1a](#).

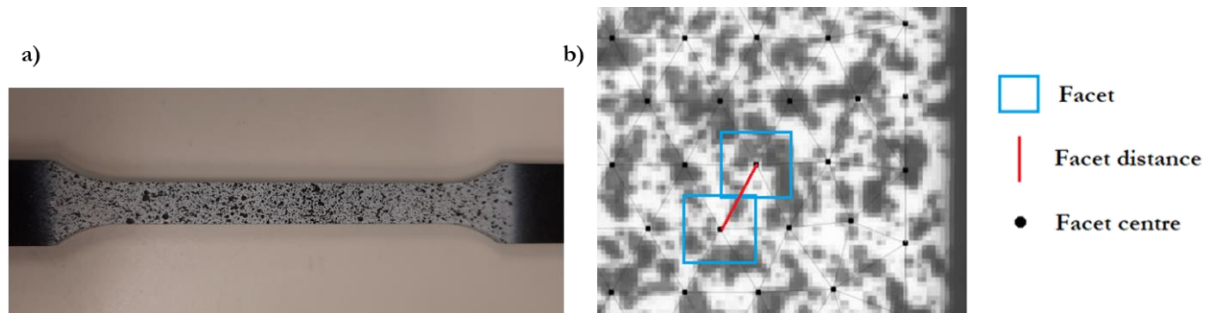


Figure 1 a) Specimen prepared for DIC technique of data extraction b) Facet points in ARAMIS interface

The ARAMIS Professional software, during its initial calibration, detects a number of square image areas on the specimen. The square image areas are called facets in the GOM software. The facets, as seen in [Figure 1b](#), are initially square and would eventually change size and shape to accommodate the pattern it encloses, as the specimen undergoes deformation. The size and the distance between the facets can be adjusted according to the need. The centre point of the facet is referred as facet centre or the facet point.

As seen in [Figure 2](#), the topology of the facet point distribution on the specimen surface is based on equilateral triangles.

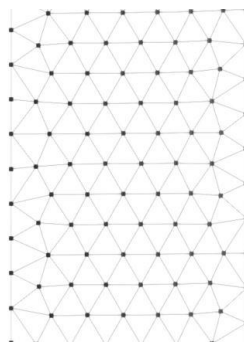


Figure 2 Facet point distribution on the surface



## 2.2 Computation of strain: Theory

Consider a continuous bar of initial length  $l_0$  under a longitudinal external force  $f_0$ . The bar deforms in the direction of the applied force and the deformation is  $\Delta l$ . The engineering or the Cauchy strain,  $\epsilon_{\text{eng}}$ , can be expressed as the magnitude of deformation in the direction of the force divided by the initial length of the bar,

$$\epsilon_{\text{eng}} = \frac{\Delta l}{l_0}.$$

The stretch ratio  $\lambda$  of a line element is defined as the ratio of current length  $l_c$  to the initial length  $l_0$ ,

$$\lambda = \frac{l_c}{l_0} = \frac{l_0 + \Delta l}{l_0} = 1 + \frac{\Delta l}{l_0} = 1 + \epsilon_{\text{eng}}.$$

Taking into account the influence of strain path, the logarithmic strain or the true strain,  $\epsilon_{\text{true}}$  can be written as,

$$\epsilon_{\text{true}} = \ln(1 + \epsilon_{\text{eng}}).$$

A material is said to be deformed if the particles within it have a relative motion to each other. In continuum mechanics, the deformation of a continuum body can be described by a second order tensor called the deformation-gradient tensor,  $\mathbf{F}$  (Spencer 2004). It can be defined as,

$$F_{iR} = \frac{\partial x_i}{\partial X_R} \text{ or } \mathbf{F} = \begin{bmatrix} F_{11} & F_{12} & F_{13} \\ F_{21} & F_{22} & F_{23} \\ F_{31} & F_{32} & F_{33} \end{bmatrix},$$

where the index  $i$  represents current configuration and  $R$  represents the reference configuration.

By the polar decomposition theorem, the non-singular square matrix  $\mathbf{F}$  can be decomposed into a product of a positive definite symmetric matrix  $\mathbf{U}$  and an orthogonal matrix  $\mathbf{R}$ . This can be denoted by,

$$\mathbf{F} = \mathbf{R} \cdot \mathbf{U}, \quad (1)$$

where the operator “ $\cdot$ ”, between two second order tensors, is defined as  $\mathbf{A} \cdot \mathbf{B} = A_{ik}B_{kj}$  and  $i, j, k = 1, 2, 3$ .  $\mathbf{R}$  is called as rotation tensor and contains the rotational part and  $\mathbf{U}$  is called as the right Stretch tensor and contains the stretch part,

$$\mathbf{U} = \begin{bmatrix} \lambda_{11} & \lambda_{12} & \lambda_{13} \\ \lambda_{21} & \lambda_{22} & \lambda_{23} \\ \lambda_{31} & \lambda_{32} & \lambda_{33} \end{bmatrix}.$$

Now consider the right Cauchy-Green deformation tensor denoted by  $\mathbf{C}$ ,

$$\mathbf{C} = \mathbf{F}^T \cdot \mathbf{F},$$

with the previous definition of  $\mathbf{F}$  as in equation (1),

$$\mathbf{C} = \mathbf{F}^T \cdot \mathbf{F} = (\mathbf{R} \cdot \mathbf{U})^T \cdot (\mathbf{R} \cdot \mathbf{U}) = \mathbf{U}^T \cdot \mathbf{R}^T \cdot \mathbf{R} \cdot \mathbf{U}.$$

Since  $\mathbf{R}$  is orthogonal meaning that  $\mathbf{R}^T \cdot \mathbf{R} = \mathbf{R} \cdot \mathbf{R}^T = \mathbf{I}$ , thus

$$\mathbf{C} = \mathbf{F}^T \cdot \mathbf{F} = \mathbf{U}^T \cdot \mathbf{U} = \mathbf{U} \cdot \mathbf{U} = \mathbf{U}^2$$

due to  $\mathbf{U}$  being symmetric, and

$$\mathbf{U} = +\sqrt{\mathbf{F}^T \cdot \mathbf{F}} = \sqrt{\mathbf{C}}$$

i.e.  $U_{ij} = \sqrt{C_{ij}}$ ;  $i, j = 1, 2, 3$ . The components of  $\mathbf{U}$  are nothing but the stretch ratios and the strains are calculated thereafter.

## 2.3 Computation of strain: Procedure

The DIC setup consists of a light source and cameras mounted on a stand. The cameras capture high resolution images of the specimen undergoing deformation during the test, for every load step. As mentioned earlier, the ARAMIS Professional software assigns small image areas called facets over the surface of the specimen. The main assumption in identifying a facet is that a casual connection exists between the original and the deformed state (GOM 2016). Through the stochastic speckle pattern, the software is able to identify the image information within the facet during each load step. With the help of coordinates of every point, the strain can be calculated in the following way.

Let us consider a material with a 2D surface which consists of one facet point. The initial coordinates of the facet point are  $(A_1, A_2)$  and the material undergoes a movement and a deformation. Let the rigid body movements along the axes be  $u_1$  and  $u_2$  and the new coordinates of the facet point be  $A'_1$  and  $A'_2$ . It can be described as,

$$\begin{bmatrix} A'_1 \\ A'_2 \end{bmatrix} = \begin{bmatrix} u_1 \\ u_2 \end{bmatrix} + \begin{bmatrix} F_{11} & F_{12} \\ F_{21} & F_{22} \end{bmatrix} \begin{bmatrix} A_1 \\ A_2 \end{bmatrix}. \quad (2)$$

Equation (2) is an underdetermined system of equations as it has two equations and six unknowns ( $u_1, u_2, F_{11}, F_{12}, F_{21}$  and  $F_{22}$ ).

Mathematically, a triangle having three points is necessary and sufficient to calculate strain. But for better support to the individual measuring points, the software also uses its neighbouring points for the calculation. Therefore, the software considers an equilateral hexagon around the facet point. Thus, the strain in the individual facet points can be calculated by solving an overdetermined system of equations.

## 3. Theory

### 3.1 Material Models in LS-DYNA

The key file, which is the input for LS-DYNA, consists of keywords which build the problem. Every keyword starts with “\*” and follows the data pertaining to the keyword. This systematically organised database enables easy understanding for the user.

The material keyword that will be used to simulate the material behaviour consists of \*MAT\_PIECEWISE\_LINEAR\_PLASTICITY and \*MAT\_ADD\_EROSION.

#### 3.1.1 MAT\_PIECEWISE\_LINEAR\_PLASTICITY

The MAT\_PIECEWISE\_LINEAR\_PLASTICITY, which is the material type 24 commonly called as \*MAT\_024, is an elasto-plastic constitutive model based on von Mises yield criterion. The input for the material model in the current application consists of mass density, Young’s modulus, Poisson’s ratio and a curve defining effective plastic strain versus effective stress.

When a specimen is under an external force  $f_0$ , perpendicular to a surface with area  $A_0$ , the engineering stress in the specimen across any cross-section perpendicular to the direction of force is given by,

$$\sigma_{\text{eng}} = \frac{f_0}{A_0}.$$

As the specimen undergoes deformation, the cross-sectional area also changes. This change in cross-sectional area is accounted by true stress in the specimen given by,

$$\sigma_{\text{true}} = \sigma_{\text{eng}}(\epsilon_{\text{eng}} + 1). \quad (3)$$

In continuum mechanics, the true stress in 3 dimensions can be expressed in terms of tensor notation and is as follows,

$$\boldsymbol{\sigma} = \begin{bmatrix} \sigma_{11} & \sigma_{12} & \sigma_{13} \\ \sigma_{21} & \sigma_{22} & \sigma_{23} \\ \sigma_{31} & \sigma_{32} & \sigma_{33} \end{bmatrix}.$$

$\boldsymbol{\sigma}$ , called as the Cauchy stress tensor, is a second order tensor which can completely define the state of stress inside a material. Since it contains stress components specified in the current configuration, it is vastly used in applications with small deformations.

The stress tensor  $\boldsymbol{\sigma}$  can be split into two parts, a hydrostatic part,  $\mathbf{p}$  and a deviatoric part,  $\mathbf{s}$ ,

$$\boldsymbol{\sigma} = \mathbf{p}\mathbf{I} + \mathbf{s},$$

where  $\mathbf{I}$  is the identity tensor. If  $\sigma_1$ ,  $\sigma_2$  and  $\sigma_3$  are the principal stresses, it is possible to choose a coordinate system such that all the non-diagonal elements of  $\boldsymbol{\sigma}$  become zero i.e.,

$$\boldsymbol{\sigma} = \begin{bmatrix} \sigma_1 & 0 & 0 \\ 0 & \sigma_2 & 0 \\ 0 & 0 & \sigma_3 \end{bmatrix},$$

which implies

$$p = \frac{1}{3}(\sigma_1 + \sigma_2 + \sigma_3) \quad (4)$$

and

$$\mathbf{s} = \begin{bmatrix} \sigma_1 - p & 0 & 0 \\ 0 & \sigma_2 - p & 0 \\ 0 & 0 & \sigma_3 - p \end{bmatrix}.$$

Herein, the second invariant  $J_2$  of the deviatoric stress tensor  $\mathbf{s}$  is defined as

$$J_2 = \frac{1}{2} s_{ij} s_{ij} = \frac{1}{6} \{(\sigma_1 - \sigma_2)^2 + (\sigma_2 - \sigma_3)^2 + (\sigma_1 - \sigma_3)^2\}. \quad (5)$$

The von Mises yield criterion states that plastic yielding will occur only when the second invariant  $J_2$  of the deviatoric stress tensor  $\mathbf{s}$  reaches a critical value  $k^2$  (Khan and Huang 1995).

The value of the material constant,  $k$  can be obtained by a simple tensile test where,

$$\boldsymbol{\sigma} = \begin{bmatrix} \sigma_1 & 0 & 0 \\ 0 & 0 & 0 \\ 0 & 0 & 0 \end{bmatrix}.$$

Hence  $J_2$  from equation (5) now becomes,

$$J_2 = \frac{\sigma_1^2}{3}.$$

For a uniaxial test, plastic yielding occurs when the stress reaches the yield value i.e.  $\sigma_1 = \sigma_y$ . Hence,

$$J_2 = \frac{\sigma_y^2}{3}.$$

And according to the von Mises yield criterion,  $J_2 - k^2 = 0$  implying that  $k = \frac{\sigma_y}{\sqrt{3}}$ . Thus, the plastic yielding takes place when the equivalent stress within the material reaches a critical yield value of stress. It can be expressed as  $\sqrt{3J_2} - \sigma_y = 0$ . In general, the yield function is given by,

$$\sigma_{vM} - \sigma_y = 0,$$

where,

$$\sigma_{vM} = \sqrt{\frac{1}{2} \{(\sigma_1 - \sigma_2)^2 + (\sigma_2 - \sigma_3)^2 + (\sigma_1 - \sigma_3)^2\}}. \quad (6)$$

The abscissa of the input load curve for the material model is effective plastic strain. In the case of uniaxial stress state, up to the point of necking, the plastic strain can be obtained by removing the elastic part of strain from the total strain. This can be expressed as,

$$\varepsilon^p = \ln(1 + \varepsilon_{\text{eng}}) - \frac{\sigma_{\text{eng}}}{E}, \quad (7)$$

where  $E$  is the modulus of elasticity. This input load curve of effective stress vs. effective plastic strain is referred to as yield curve in this report. The elasto-plastic material model follows an isotropic hardening description described by

$$\sigma_{yI} = \beta[\sigma_0 + f_h(\varepsilon_{\text{eff}}^p)],$$

where  $\sigma_{yI}$  is the instantaneous yield stress; since in isotropic hardening description, the radius of the yield surface changes.  $\sigma_0$  is the initial yield stress and the hardening function  $f_h(\varepsilon_{\text{eff}}^p)$  can be specified in the form of a table (Hallquist 2006).  $\varepsilon_{\text{eff}}^p$  is the effective plastic strain. Let  $\Phi$  be the yield function and the plastic flow rule can be written as

$$\Delta \varepsilon_{ij}^p = \frac{\left(\frac{3}{2} s_{ij}^* s_{ij}^*\right)^{\frac{1}{2}} - \sigma_{yI}}{3G + E_p} \frac{\partial \Phi}{\partial \sigma_{ij}},$$

where  $G$  and  $E_p$  are shear and current plastic hardening moduli, respectively. The asterisk in  $s_{ij}^*$  represents trial state.

### 3.1.2 MAT\_ADD\_EROSION

The damage model GISSMO (Generalised Incremental Stress–State dependent damage Model) was originally formulated for its application in crashworthiness simulations. The model was developed at Daimler and DYNAmore (Effelsberg, Haufe et al. 2012). It was mainly developed to overcome the limitations of the forming limit curve, which does not consider a possible change in strain path during a forming process (Neukamm, Feucht et al. 2009). With the usage of GISSMO, the damage accumulation due to plastic deformation during sheet metal forming can be introduced into crashworthiness simulations as a history data. This will result in the improvement of predictiveness of crashworthiness simulations. The intention was to have a user-friendly input of material parameters achieved by phenomenological formulation of ductile damage. It is not a complete constitutive model and hence needs to be coupled with a plasticity model. In this thesis, \*MAT\_ADD\_EROSION will be coupled with \*MAT\_PIECEWISE\_LINEAR\_PLASTICITY.

During the late 1960s, extensive studies by means of micro-mechanics analysis had been carried out on ductile plastic damage<sup>‡</sup> (Lemaitre 1985). The studies resulted in a good representation of physical mechanisms at microscale, but had its limitations when the analyses were implemented to predict failure in large scale structures. The continuous damage mechanics approach deals with the introduction of a damage variable and an effective stress concept in the structural calculation.

Consider a continuum which has undergone plastic deformation. A volume element with cross section area,  $A$  defined by its normal,  $\mathbf{n}$  is depicted in Figure 3. The body is now damaged and microcracks and voids have been formed. Let  $A_D$  be the total area of the microcracks and voids in

---

<sup>‡</sup> The phenomenon of initiation and growth of cavities and microcracks induced by large deformations in metals was referred as ductile plastic damage.

the same cross section. Let  $\tilde{A}$  be the effective area that has a load bearing capacity. The damage variable  $D_{\mathbf{n}}$  that is associated with the normal  $\mathbf{n}$  can now be introduced as,

$$D_{\mathbf{n}} = \frac{A - \tilde{A}}{A}.$$

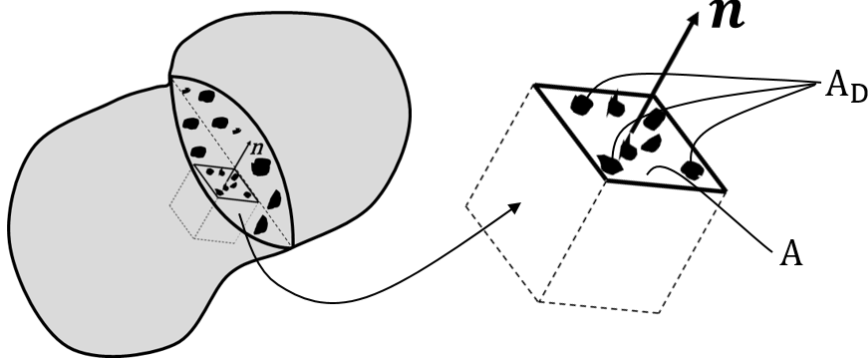


Figure 3 A volume element in a deformed body

Restricting to isotropic damage, where the voids and cracks are equally distributed in all directions,  $D_{\mathbf{n}}$  can be written as a scalar  $D$  i.e.,

$$D = D_{\mathbf{n}}.$$

Using this relation, the effective area can be written as,

$$\tilde{A} = A(1 - D).$$

If  $\mathbf{f}$  is a load acting on a given section  $A$ , then the traction vector can be given by,

$$\mathbf{t} = \frac{\mathbf{f}}{A}.$$

Similarly, for a section  $\tilde{A}$ ,

$$\tilde{\mathbf{t}} = \frac{\mathbf{f}}{\tilde{A}}.$$

Inserting the expression for effective area in the above equation yields,

$$\tilde{\mathbf{t}} = \frac{\mathbf{t}A}{A(1-D)} = \frac{\mathbf{t}}{(1-D)}. \quad (8)$$

The Cauchy stress theorem yields  $\boldsymbol{\sigma} \cdot \mathbf{n} = \mathbf{t}$ . Since  $D$  is a scalar, equation (8) can be written as,

$$\tilde{\boldsymbol{\sigma}} = \frac{\boldsymbol{\sigma}}{(1-D)}. \quad (9)$$

[Bridgman \(1952\)](#) was one of the pioneers who, with his wide range of experiments on numerous materials, illustrated the effect of hydrostatic pressure on fracture strain. Later during 1960s and 1970s, the claim was further investigated and asserted by many. A stress-state indicator was then proposed using the invariants of stress tensor and equivalent measure of stress. With the help of this parameter, nowadays widely known as triaxiality, one can predict the stress state in an isotropic material under plane stress condition. Even though the triaxiality alone is sufficient to determine stress-state in an isotropic material under plane stress, for three-dimensional stress-state the so-

called lode angle is also necessary in addition to the aforementioned. The triaxiality,  $\eta$  is defined as the ratio of hydrostatic stress and equivalent stress.

$$\eta = \frac{\sigma_H}{\sigma_{eq}}, \quad (10)$$

where the hydrostatic stress,  $\sigma_H$  is the first invariant of the Cauchy stress tensor,  $\boldsymbol{\sigma}$  and  $\sigma_{eq}$  can be von Mises stress as described in section 3.1.1. In a broader perspective, the stress-state in an element will not be the same when under a non-proportional loading. Thus, the GISSMO model should be able to account for the change in strain path and therefore the need for an incremental treatment of instability<sup>§</sup> and damage. Weck, Wilkinson et al. (2006), through their measurements on model materials, illustrated that the strain and the damage, in the form of void growth, are related exponentially. Therefore an assumption was made regarding both damage,  $D$  and measure of instability,  $F$ , and a non-linear means of accumulation was formulated.

$$\Delta F = \frac{n * F^{(1-\frac{1}{n})}}{\epsilon_{crit}(\eta)} \Delta \epsilon^p$$

and

$$\Delta D = \frac{n * D^{(1-\frac{1}{n})}}{\epsilon_f(\eta)} \Delta \epsilon^p,$$

where  $\Delta \epsilon^p$  is an increment in plastic strain for which an increment in measure of instability,  $\Delta F$  and an increment in damage parameter,  $\Delta D$ , are calculated.  $\epsilon_f(\eta)$  and  $\epsilon_{crit}(\eta)$  are the equivalent plastic strain to failure and equivalent plastic strain to instability, as a function of triaxiality, respectively.  $n$  is the damage exponent and a value of  $n=1$  results in linear accumulation. If GISSMO is activated, the values of  $F$  and  $D$  are calculated for each time step as soon as the elements enter the plastic regime. When the value of  $F$ , computed incrementally through  $\Delta F$ , becomes equal to 1, a coupling of damage and stress is expected to occur. The value of  $D$  when  $F$  reaches unity is considered as the damage threshold  $D_{crit}$ . As  $D$  reaches the threshold value  $D_{crit}$ , the stress tensor,  $\boldsymbol{\sigma}$ , and the damage are coupled and thus the effective stress tensor,  $\tilde{\boldsymbol{\sigma}}$ , is calculated according to:

$$\boldsymbol{\sigma} = \tilde{\boldsymbol{\sigma}} \left[ 1 - \left( \frac{D - D_{crit}}{1 - D_{crit}} \right)^m \right], \quad (11)$$

where  $m$  is the so-called fading exponent. The fading exponent influences on the amount of energy that is dissipated when the element fades out. For a value of  $m=1$  and  $D_{crit}=0$  in equation (11), the Lemaitre's equation as in equation (9) is restored.

One needs to appreciate the fact that a spurious mesh dependence (Andrade, Feucht et al. 2014) will be present during an event such as localization, when the strain is not uniform. The element strain is also a function of element size and different mesh size will yield different simulation results. This mesh dependency should not be confused with the one that causes inaccurate results because of coarse mesh. In GISSMO, there is a possibility to introduce element size dependent factors which can adjust the softening part of the response curve according to the corresponding element size. This method does not directly solve the problem of mesh dependence but compensates for

---

<sup>§</sup> In the present context, instability can be seen as the onset of softening through localization.

its effect in calculation of damage. To achieve this in the model, one needs to feed in a load curve defining scale factors of equivalent plastic strain to failure for corresponding element sizes.

## 3.2 Optimization

### 3.2.1 Response Surface Methodology

Consider an experiment consisting of two input variables  $\alpha_1$  and  $\alpha_2$  generating an output or a response,  $z$ . The input variables,  $\alpha_1$  and  $\alpha_2$ , are also called independent variables and  $z$  is called as the response variable. For each value of input variables there is a corresponding value of response, which can be represented graphically as seen in [Figure 4](#).

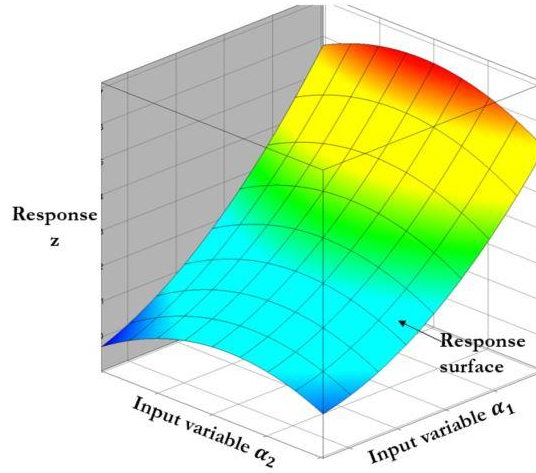


Figure 4 An example for a response surface

The surface in the [Figure 4](#) is called as response surface and it is this graphical perspective of the problem environment that led to the term “Response Surface Methodology (RSM)”. The field of RSM consists of experimental strategies for exploring the space of the independent variables, empirical statistical modelling to develop an appropriate approximating relationship between the responses and the independent variables, and optimization methods for finding the values of the independent variables that produce a desirable value of the response variables ([Myers, Montgomery et al. 2016](#)).

The relationship between the response,  $z$  and the independent variables,  $\alpha_1$  and  $\alpha_2$  can be written as,

$$z = f(\alpha_1, \alpha_2) + \epsilon_e,$$

where the term  $\epsilon_e$  represents a source of variability not represented in the true response function  $f(\alpha_1, \alpha_2)$ . It is considered as a statistical error having normal distribution with mean zero and variance  $S^2$ , where  $S$  is the standard deviation. Therefore,

$$E(z) \equiv \varphi = E[f(\alpha_1, \alpha_2)] + E(\epsilon_e).$$



Since the mean of  $\epsilon_e$  is zero,  $E(\epsilon_e) = 0^{**}$ . Hence,

$$\varphi = f(\alpha_1, \alpha_2).$$

Since the true response function,  $f(\alpha_1, \alpha_2)$  is unknown and complicated to determine, a suitable approximation could be developed.  $\alpha_1$  and  $\alpha_2$ , called as natural variables, can be transformed to coded variables,  $y_1$  and  $y_2$ , which are dimensionless with mean zero and variance  $S^2$ ; and can be written as,

$$\varphi = f(y_1, y_2).$$

Since the form of the true response function  $f(y_1, y_2)$  is unknown, it needs to be approximated (Myers, Montgomery et al. 2016). An example for a first-order model with the aforementioned independent variables in terms of coded variables is as follows,

$$\varphi = \beta_0 + \beta_1 y_1 + \beta_2 y_2.$$

This is a multiple linear regression model which can be generalised to a number of experiments yielding a number of responses.

Let  $y_{ij}$  denote the  $i^{\text{th}}$  observation or experiment of an independent variable  $y_j$ ,  $i = 1, 2, \dots, P$ ;  $j = 1, 2, \dots, K$ ;  $P$  represents the number of experimental points and  $K$  represents the number of independent variables. The error term  $\epsilon$  in the model has mean zero and variance  $\sigma^2$  and  $\{\epsilon_i\}$  are uncorrelated random variables. The response variable for each observation can be written as,

$$z_i = \beta_0 + \beta_1 y_{i1} + \beta_2 y_{i2} + \dots + \beta_K y_{iK} + \epsilon_i$$

or

$$z_i = \beta_0 + \sum_{j=1}^K \beta_j y_{ij} + \epsilon_i. \quad (12)$$

A method of least square is chosen to minimize the sum of squares of the errors  $\epsilon_i$  in equation (12) and can be expressed as,

$$L = \sum_{i=1}^P \epsilon_i^2$$

i.e.

$$L = \sum_{i=1}^P (z_i - \beta_0 - \sum_{j=1}^K \beta_j y_{ij})^2.$$

Let  $\phi_i = \beta_0 + \sum_{j=1}^K \beta_j y_{ij} = \sum_{q=0}^K \beta_q y_{iq}$  such that  $y_{i0} = 1$  and  $q = 0, 1, \dots, K$ . The function  $\phi_i$  is called a basis function. Equation (12) can be written in matrix form as,

$$\mathbf{z} = \mathbf{Y}\boldsymbol{\beta} + \boldsymbol{\epsilon},$$

where,

---

<sup>\*\*</sup>  $E(\epsilon_e)$  is the expectation of  $\epsilon_e$ .

$$\mathbf{z} = \begin{Bmatrix} z_1 \\ z_2 \\ \vdots \\ z_P \end{Bmatrix}; \mathbf{Y} = \begin{bmatrix} 1 & y_{11} & y_{12} & \dots & y_{1K} \\ 1 & y_{21} & y_{22} & \dots & y_{2K} \\ \vdots & \vdots & \vdots & \ddots & \vdots \\ 1 & y_{P1} & y_{P2} & \dots & y_{PK} \end{bmatrix}; \boldsymbol{\beta} = \begin{Bmatrix} \beta_0 \\ \beta_1 \\ \vdots \\ \beta_K \end{Bmatrix}; \boldsymbol{\varepsilon} = \begin{Bmatrix} \varepsilon_1 \\ \varepsilon_2 \\ \vdots \\ \varepsilon_P \end{Bmatrix}.$$

The solution to the minimization problem, which is the least square estimation  $\mathbf{b}$ , to  $\boldsymbol{\beta}$  (Roux, Stander et al. 1998) is found with,

$$\mathbf{b} = (\mathbf{Y}^T \mathbf{Y})^{-1} \mathbf{Y} \mathbf{z}.$$

LS-OPT allows linear, elliptic, linear with interaction and quadratic basis functions.

After the selection of basis function, the next step is to choose a method for selection of points in the design space. The points selected will be considered for evaluation of the response. This method is commonly called as design of experiments. One can achieve higher accuracy and lower cost of building the response surface by carefully choosing the experimental design. There is a possibility of using built-in point selection method such as D-optimal, factorial, Koshal, composite and five others in LS-OPT. It also allows user defined point selection.

The material parameters are optimised in LS-OPT by adopting the method of nonlinear regression<sup>††</sup>. The material parameters can be identified by matching the experimental behaviour to the simulation response. In LS-OPT, this can be achieved by using curve matching metrics as the minimization objective. The software has four curve matching techniques out of which two are used in this thesis.

### 3.2.2 Mean Square Error

Mean Square Error (MSE) option in LS-OPT is an ordinate-based error measurement technique which calculates the Euclidean distance between the experimental and the computational results. Consider a set of experimental points  $E_n(\mathbf{z})$  which can be interconnected to form a curve  $E(\mathbf{z})$ . The independent variable,  $\mathbf{z}$  in this example, represents a physical quantity. The response curve from the simulation will consist of  $f(\mathbf{t})$  and  $\mathbf{z}(\mathbf{t})$ . The variable  $\mathbf{t}$  represents time and the function  $f(\mathbf{t})$  and  $\mathbf{z}(\mathbf{t})$  are physical quantities that are the ordinate and abscissa of the experimental graph, respectively. A built-in crossplot feature can be used to obtain the curve  $f(\mathbf{z})$ . The intermediate points could be obtained by interpolation.

During an optimization for an unknown parameter  $\mathbf{x}$  in the parameter space, the response curve  $f(\mathbf{x}, \mathbf{z})$  is obtained. The MSE norm  $\varepsilon_{\text{MSE}}$  (Stander, Basudhar et al. July 2019) between the two curves for  $N$  regression points can be expressed as,

$$\varepsilon_{\text{MSE}} = \frac{1}{N} \sum_{n=1}^N W_n \left( \frac{f_n(\mathbf{x}) - E_n}{s_n} \right)^2,$$

where  $W$  is a set of weights and  $s$  is a set of residual scale factors and  $n = 1, \dots, N$ .

---

<sup>††</sup> Nonlinear regression is a form of regression analysis where the observational data is modelled by a nonlinear equation consisting of model parameters and one or more independent variables.

MSE similarity measure has a few drawbacks. It is difficult to implement when the curves are steep or the horizontal ranges for comparison are not same. The latter drawback would lead to some of the points not being considered.

### 3.2.3 Dynamic Time Warping

Dynamic Time Warping (DTW), first introduced in 1960s, became popular in 1970s through its application in speech recognition. LS-OPT uses a normalised DTW approach where the DTW value is normalised by the length of the warping path. Consider two different set of points  $B$  and  $C$  forming two polygonal chains. Let  $B = (b_1, \dots, b_n)$  and  $C = (c_1, \dots, c_m)$ . Let  $d(\cdot, \cdot)$  denote Euclidean distance between two points. Let  $W$  be the warping path between  $B$  and  $C$  and  $W = (w_1, \dots, w_l)$ . For instance if  $w_i = (h, v)$  where  $h \in 1, \dots, n$ ,  $v \in 1, \dots, m$  and  $i \in 1, \dots, l$ , then the normalised DTW distance (Stander, Basudhar et al. July 2019) can be calculated as follows,

$$DTW(B, C) = \frac{1}{l} \min_W \{ \sum_{i=1}^l \delta(w_i) \},$$

where  $\delta(w_i) = d(b_h, c_v)$ .

A major drawback with DTW is that it compares all the points on the curve and heavy noise at one part can lead to a poor solution. Also, it is suggested by the software supplier to use equal density of points which are uniformly spaced on both the curves. This can be achieved by the built-in capability of LS-OPT to interpolate between the curves.

A simple example of how the DTW algorithm finds the warping path that accumulates a minimum ordinate distance between two curves is illustrated in Appendix 1: Example: DTW.

### 3.3 Three-point bending

Consider a rectangular cross section simple determinate beam of thickness,  $t$  and depth,  $d$ . The beam is simply supported on either end of its span of length  $l$ . Let a point load,  $q$  be acting on its centre point along the vertical direction as seen in Figure 5a. The reaction force at the supports are shown in Figure 5b. The maximum bending moment experienced by the beam is at the centre of the span and therefore the beam is expected to undergo maximum deflection at the same point.

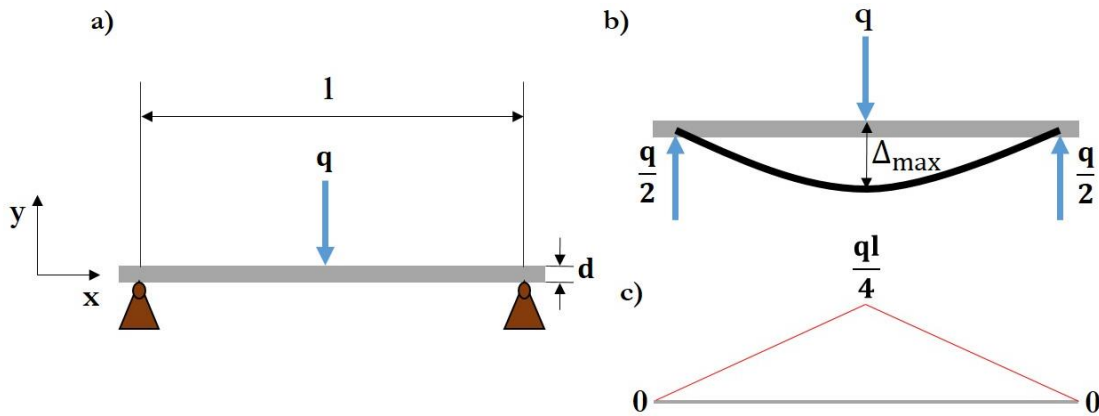


Figure 5 A schematic representation of a) the beam with b) reaction forces and c) bending moment diagram for a three point bending scenario

The flexure formula (Hopkins, Patnaik et al. 2003) for a beam under pure bending is given by,

$$\frac{-\sigma}{y} = \frac{M}{I}, \quad (13)$$

where  $\sigma$  is the normal stress induced by the bending moment,  $M$ .  $y$  is the distance from the neutral axis along the  $y$ -direction. Negative values of  $y$  indicate the positions below the neutral axis and vice-versa. The lowermost fiber which is at a distance,  $y = -\frac{d}{2}$  undergoes the maximum tension as the value of  $\sigma$  in equation (13) becomes positive. Similarly, the uppermost fiber undergoes the maximum compression. Area moment of inertia  $I$ , for a rectangular section is given by,

$$I = \frac{td^3}{12}.$$

Considering the elastic regime, Hooke's law states that  $\sigma = E\varepsilon$ . Inserting in the equation (13) and rearranging the terms yield,

$$\varepsilon = -\frac{My}{EI}. \quad (14)$$

According to the assumptions of the beam theory and geometric relationships (Hopkins, Patnaik et al. 2003), a relation between normal strain ( $\varepsilon$ ) and transverse displacement ( $v$ ) can be formulated as,

$$\varepsilon = -y \frac{d^2v}{dx^2}.$$

Inserting the above equation in equation (14) yields,

$$\frac{d^2v}{dx^2} = \frac{M(x)}{EI}. \quad (15)$$

Since the bending moments on either side of the load is different, the vertical deflection (or the displacement function) of the beam can be written for two different segments.  $M(x)$  is a function that defines the variation of moment in the corresponding section of the beam. Integration of equation (15) and solving for the constants with appropriate boundary conditions, for each segment of the beam yields,

$$v(x) = \begin{cases} \frac{qx}{48EI} (4x^2 - 3l^2) & \text{for } 0 \leq x \leq \frac{l}{2} \\ \frac{qlx}{48EI} \left( 12x - \frac{4x^2}{l} - 9l + \frac{l^2}{x} \right) & \text{for } \frac{l}{2} \leq x \leq l \end{cases}$$

The maximum deflection is expected at the center point where  $x = \frac{l}{2}$  and the magnitude of deflection is given by,

$$\Delta_{\max} = \frac{ql^3}{48EI}. \quad (16)$$

### 3.4 Four-point bending

A four-point bending consists of a similar setup as the three-point bending, but there are two symmetric point loads acting at a distance from the centre point (see Figure 6a).

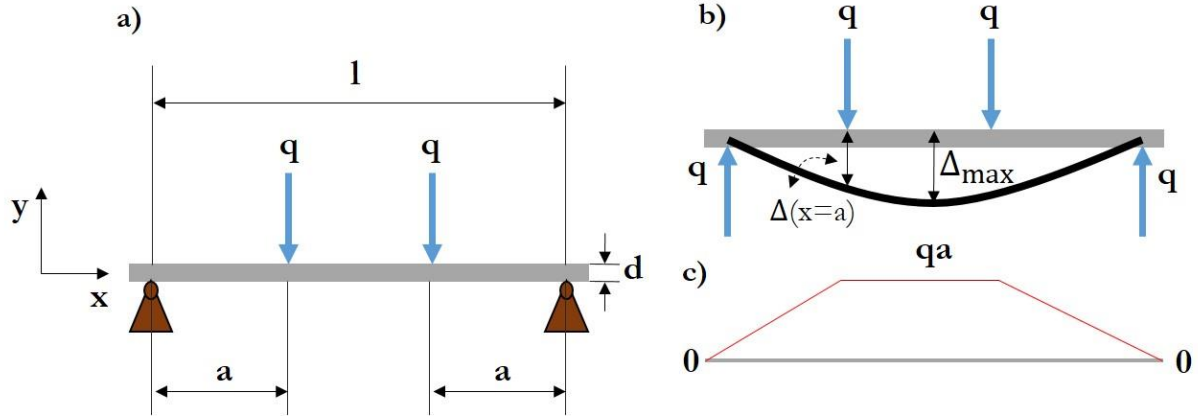


Figure 6 A schematic representation of a) the beam with b) reaction forces and c) bending moment diagram for a three point bending scenario

The maximum bending moment is experienced by the beam at the region between the two point loads. A schematic representation of a deformed beam can also be seen in Figure 6b. Through the formulation of moment equations for each of the three segments of the beam, one can obtain the deflection formulas as discussed in the previous section. It must also be noted that the deflection is symmetric about the center point. The transverse displacement equations for the first two segments from the left is given by,

$$v(x) = \begin{cases} \frac{qx}{6EI}(-3la + x^2 + 3a^2) & \text{for } 0 \leq x \leq a \\ \frac{qa}{6EI}(-3lx + 3x^2 + a^2) & \text{for } a \leq x \leq (l-a) \end{cases}$$

The deflection at the point where the load acts is given by,

$$\Delta(x = a) = \frac{qa^2}{6EI}(3l - 4a). \quad (17)$$

The maximum deflection of the beam is expected to occur at the centre point and is given by,

$$\Delta_{\max} = \frac{qa}{24EI}(3l^2 - 4a^2).$$

These formulas can be derived or are readily available in most of the solid mechanics handbooks, such as the one by Björk (2007).

For convenience, let a testing machine control the movement of the loading pins and it exerts a force  $Q$  such that  $2q = Q$ . Equation (17) can then be written in terms of the force exerted by the machine as,

$$\Delta(x = a) = \frac{Qa^2}{12EI}(3l - 4a). \quad (18)$$

## 4. Method

### 4.1 Material parameter identification

The process of material parameter identification, in general, is explained in this section with the help of a flow chart (see Figure 7). Experiments are conducted on the standard specimens and suitable data are extracted during the experiment. An accurate model of the specimen is built in a finite element software. App boundary conditions are applied on the model to replicate the physics during the experiment. A similar response is extracted from the simulation. A comparison is made between experimental data and the simulation response. In case of curves, an appropriate similarity measure is chosen to quantify the difference between two curves. The experimental curve is considered as target curve and the parameters in the simulation can be tweaked to reduce the difference with target curve. This is achieved with the help of LS-OPT, which is an optimization software. The difference between the curves is also referred as distance functional. The optimization is carried out with an objective to minimize the distance functional. The output from the optimization will be the optimal value of material parameters that mimic the material behaviour as in the experiment.

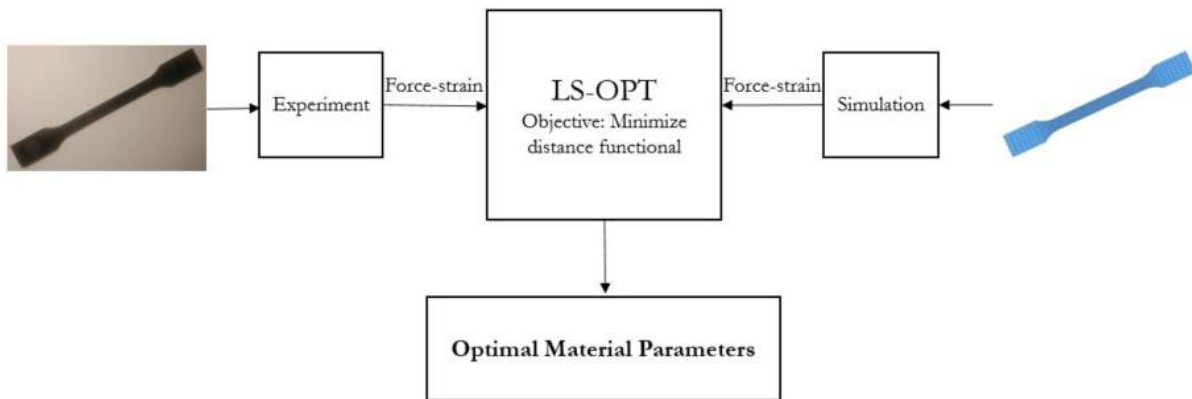


Figure 7 Flow chart describing a material parameter identification process

### 4.2 Material testing

The experimental tests were carried out at IKEA Test Lab, Älmhult. Uniaxial tensile tests were conducted on dumb-bell-shaped test specimens of type 1A according to ISO 527-2 (2012). The geometric specification of a specimen of type 1A can be seen in Figure 8. In this thesis, the tensile test on each specimen was carried out at 2 different speeds, 1 millimetre per minute and 50 millimetres per minute. The initial part of test was carried out at a grip speed of 1 millimetre per minute, to have a high density of data points for the calculation of derived physical quantities such as Young's modulus and Poisson's ratio.

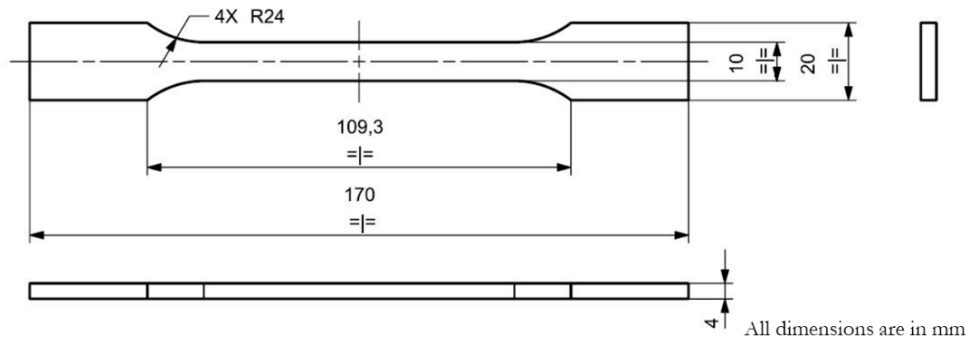


Figure 8 Geometric specifications of the specimen

The tests were carried out on five specimens, each made of 30 % glass fibre reinforced thermo-plastic material. The most generic test sample, with a value closest to the mean value of physical quantities determined according to IKEA's in-house scripts<sup>##</sup>, was considered for further investigations as the target curve or the experimental curve. The specimens were prepared as described in section 2.1 to enable optical non-contact measurement through the DIC system by GOM. The initial setup consists of ARAMIS 3D camera, light projector and sensor mounted on a stand as seen in Figure 9. The setup is connected to ARAMIS Professional software installed on a computer. The stereo camera setup enables measurement in 3D. The system measures 3D coordinates of the facet points during the deformation. From the 3D coordinates, quantities such as strain, displacement, velocity can be derived as discussed in section 2.2. The initial image captured will be considered as reference state for measurements.

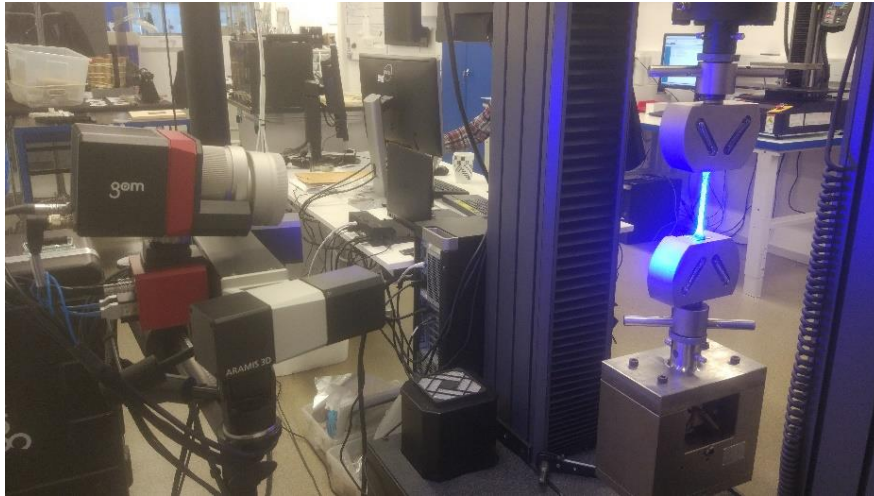


Figure 9 DIC setup during the experiment

Mainly, two types of force-true strain data, as seen in Figure 10, were extracted from the experiment. A virtual extensometer of 75 mm gauge length was used in ARAMIS Professional, to obtain the force-true strain data across the 75 mm gauge length. This would constitute a conventional method of extracting data from the experiments and will be further associated with the term Regular routine. A major advantage of DIC technique is that it is possible to obtain the data from each

---

<sup>##</sup> The Script imports material parameters and their corresponding weights, that are chosen by the operator, and determines the most generic test sample based on the mean value among the test samples.



facet point, in the region between two extreme ends of the virtual extensometer. A graph of force against the corresponding true strain data, from all facet points, for the consecutive load stages, is a mathematical entity that represents both spatial and temporal dimensions. This type of output from the ARAMIS Professional software will be further associated with the term FFC routine.

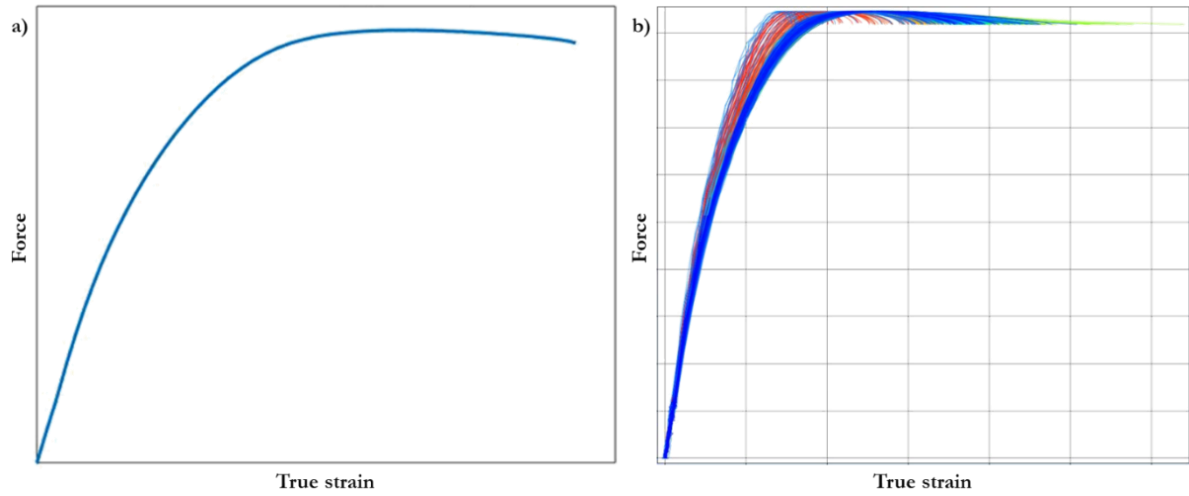


Figure 10 Experimental data extracted from a) 75 mm gauge length extensometer b) DIC system

In addition to the tensile test, bending tests were also conducted on the specimen, to validate the material model obtained from calibration against the tensile test in LS-OPT. Both three-point and four-point bending tests were carried out on five specimens each. The most generic specimen (see [Appendix 2: Generic specimen from bending tests](#)), closest to the mean value of the ordinate in force-displacement graphs, was chosen from each experiment. The setup for the four-point bending test, with its geometric data, is provided in [Figure 11](#). For the three-point bending test, one loading pin is used, which is placed in the centre between the supports. The tests were carried out at the loading pin's vertical translation speed of 50 millimetres per minute, to achieve quasi-static condition. This was done as to elude the possibility of strain-rate dependence on material behaviour and to have uniform speed in all the tests.

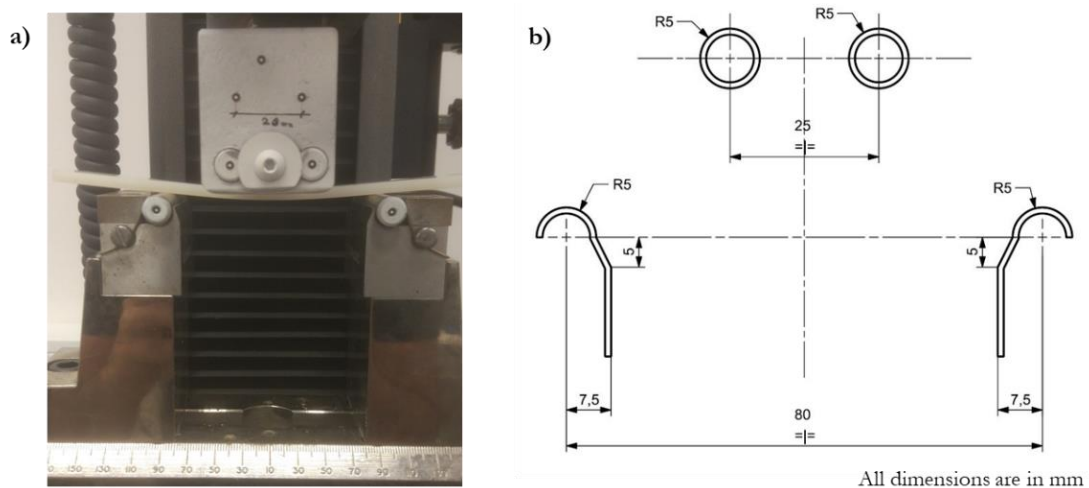


Figure 11 The a) setup with its b) geometrical specification for the four-point bending



### 4.3 Modelling in LS-PrePost

A CAD geometry of the dumb-bell shaped test specimen was imported into HyperMesh. It is first meshed on the surface with 2D quadrilateral elements and then with the line drag option along the thickness. Thus, a finite element (FE) model of the specimen, built up with hexahedron elements, was generated. The FE model was imported into LS-PrePost for pre-processing. The FE model was split into three parts, as seen in Figure 12, so that the portion of the specimen held by the grips was considered as rigid. The parts were made rigid through the usage of keyword `*MAT_RIGID`.

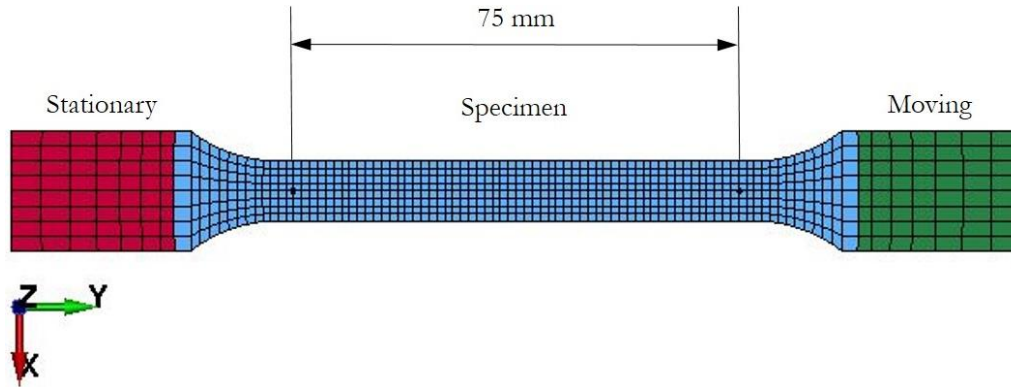


Figure 12 The FE model

An advantage of using `*MAT_RIGID` is that the elements that are modelled as rigid are bypassed during element processing and no storage is allocated for storing history variables, therefore being cost efficient in a simulation (LSTC 2017). The stationary part was constrained in all direction translations and rotations. The moving part was constrained in all directions except y-axis translation which is the longitudinal direction of the specimen. The movement of the grip, resulting in elongation of the specimen, during the experiment was mimicked in the FE simulation by applying translational motion to the moving part along the y-axis. This was achieved with the help of `*BOUNDARY_PRESCRIBED_MOTION_RIGID` keyword, that allows to prescribe a load curve defining velocity of rigid body motion against time, applied on the moving part. Since explicit time integration was chosen to solve time dependent differential equations, the time step needed to be very small. To reduce the overall simulation time, a higher loading rate was used. But, for a quasi-static analysis, the first Eigenmode is dominant and it is suggested, by DYNAmore Nordic AB, that the loading period must be at least 10 times the time period of first mode. A Smooth curve of displacement against loading time was generated using CurveGen option. The curve was then differentiated to obtain a curve of velocity against loading time.

Fully integrated S/R (Selective Reduced) solid elements (ELFORM 2) were used for modelling the test specimen. A cross section set was created with the keyword `*DATABASE_CROSS_SECTION_SET` to extract the section force. Two nodes, constituting the extreme points of a 75 mm gauge length extensometer, were selected to extract displacement data, therefore to calculate extensometer displacement during the simulation.

The linear elastic and non-linear hardening behaviour could be modelled with the elasto-plastic material model with von Mises yield criterion, widely known as `*MAT_PIECEWISE_LINEAR_PLASTICITY` in LS-DYNA. The input parameters for this material model are described in the section 3.1.1. Among the four inputs that are mentioned, mass density and Poisson's ratio can

be considered to remain constant during the optimization. The Young's modulus of elasticity can be treated as an independent variable or a model parameter, along with the yield curve, during the optimization to achieve target material behaviour. In LS-DYNA, a real number input can be set as a parameter through the keyword \*PARAMETER. The yield curve input, which is a table consisting of values of effective plastic strain against the corresponding effective stress, can be parameterised through a modified version of Hockett-Sherby equation (Hockett and Sherby 1975). The modified version of the Hockett-Sherby equation constructs a relation between true stress and plastic strain as,

$$\sigma_{\text{true}}(\epsilon^p) = A \left( 1 - e^{-C\epsilon^{pN}} \right) + B e^{-C\epsilon^{pN}}.$$

It must also be noted that, for a uniaxial stress state, the yield curve can be directly obtained from the experimental data through equations (3) and (7). The usage of an equation, such as the Hockett-Sherby equation, to parametrize the yield curve can be motivated as the presence of non-uniformity in strain in the hardening part of the DIC data. The same approach was implemented in the regular routine to ensure similarity between the routines and identical treatment of input data. The variables A, B, C and N can be used as model parameters during the optimization. A general example of how a yield curve looks like is shown in Figure 13a.

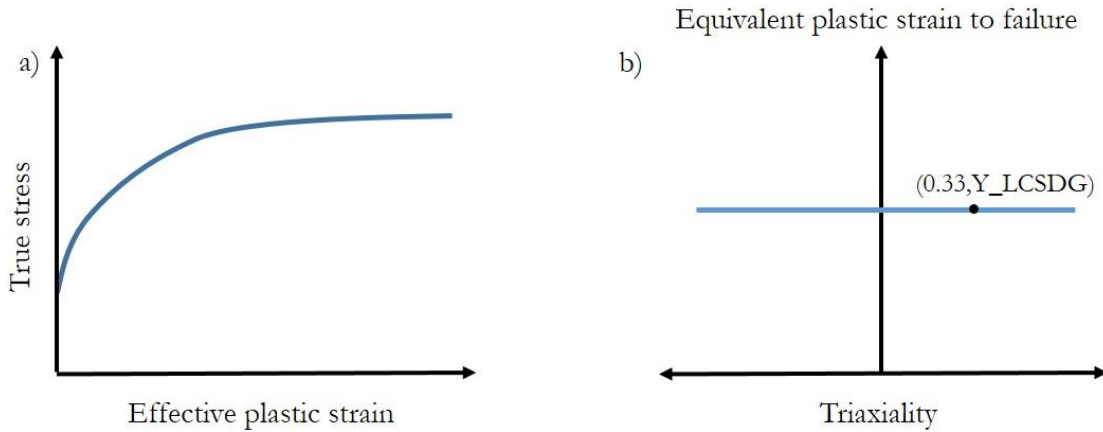


Figure 13 An example of a) Yield curve b) LCSDG curve

The softening behaviour after the necking point, leading to failure can be modelled using \*MAT\_ADD\_EROSION keyword. The GISSMO damage model, described in section 3.1.2, can be activated by setting IDAM to 1. For the current application, equivalent plastic strain to instability (ECRIT), damage exponent (DMGEXP) and fading exponent (FADEXP) were considered to be the model parameters. In addition to the three parameters mentioned before, a load curve defining equivalent plastic strain to failure vs. triaxiality (LCSDG) has to be given as an input. For a uniaxial loading case, the value of the triaxiality can be calculated through equations (4), (6) and (10) as,

$$\eta = \frac{\sigma_H}{\sigma_{eq}} = \frac{\frac{(\sigma_1 + 0 + 0)}{3}}{\sqrt{\frac{(\sigma_1^2 + 0 + \sigma_1^2)}{2}}} = \frac{1}{3}.$$

A general example of LCSDG curve for a uniaxial loading case can be seen in Figure 13b. The y-coordinate of the LCSDG curve will be hereinafter referred to as Y\_LCSDG. Softening behaviour is attained by coupling of damage to the stress through equation (11). Therefore, it is necessary to extrapolate the yield curve beyond the necking point. The built-in extrapolation is a straight-line

extrapolation with a slope equal to the slope between the two previous points. To have a curve, whose shape can be controlled in the form of a model parameter, was possible through the implementation of a cubic Hermite spline interpolation between the points A and B as depicted in Figure 14. The usage of such a spline for extrapolation, also allows to satisfy  $C_1$ -continuity at the transition point (necking point). In addition to this, it is possible to change the shape of the curve unlike the straight-line extrapolation. With this ability of the cubic Hermite spline, the probability of achieving a better fit with the softening part of the experimental curve increases.

Let the points A and B, seen in Figure 14, have coordinates  $(X_p, Y_p)$  and  $(X_{p+1}, Y_{p+1})$ , respectively. Let  $m_p$  and  $m_{p+1}$  be the slope at point A and B. Equation of the spline interpolating between points A and B, is given below,

$$y_i = h_{00}(t)Y_p + h_{10}(t)m_p(X_{p+1} - X_p) + h_{01}(t)Y_{p+1} + h_{11}(t)m_{p+1}(X_{p+1} - X_p),$$

where  $h_{00}$ ,  $h_{10}$ ,  $h_{01}$  and  $h_{11}$  are the four Hermite basis functions defined as,

$$h_{00}(t) = 2t^3 - 3t^2 + 1,$$

$$h_{10}(t) = t^3 - 2t^2 + t,$$

$$h_{01}(t) = -2t^3 + 3t^2,$$

$$h_{11}(t) = t^3 - t^2.$$

And

$$t = \frac{(x_i - X_p)}{(X_{p+1} - X_p)},$$

where  $x_i$  and  $y_i$  are the coordinates of  $i^{\text{th}}$  interpolation point between A and B.

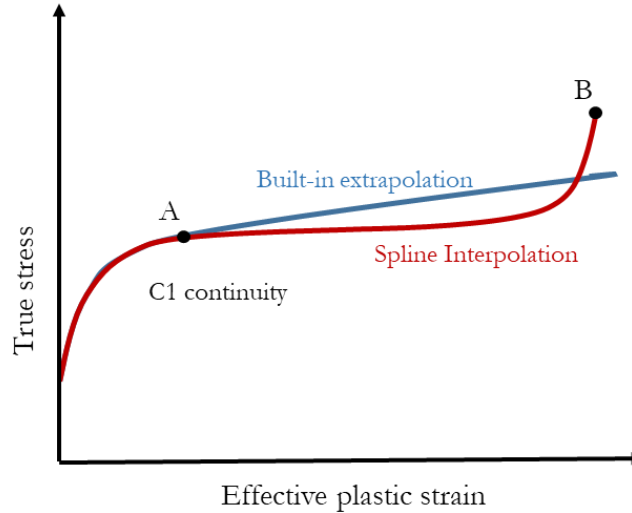


Figure 14 A cubic Hermite spline interpolation between points A and B

To satisfy  $C_1$ -continuity, the slope and coordinates at point A needs to be kept constant. It has been noted that the slope at point B,  $m_{p+1}$ , itself is enough to change the shape of the spline. Hence, the coordinates of point B were considered constant and the slope at point B, hereinafter

referred to as END\_SLOPE, was considered as a model parameter. The list of model parameters associated with the calibration of each material card can be seen in [Table 1](#).

Model parameters	
*MAT_024	*MAT_ADD_EROSION
Young's modulus	ECRIT
A	DMGEXP
B	FADEXP
C	Y_LCSDG
N	END_SLOPE

Table 1 Model parameters for the optimization

The three-point and four-point bending setups were modelled in LS-PrePost with the geometric data as illustrated in [Figure 11](#). The supporting pins are common in both type of tests and were modelled with shell elements. The keyword \*MAT\_RIGID was used and ELFORM 2 was used for shell elements, which is the default. ELFORM 2 refers to Belytschko-Lin-Tsay shell element which is based on a combined co-rotational and velocity-strain formulation ([Hallquist 2006](#)). Bilinear shape functions are used and Mindlin theory of plates and shells is adopted to partition the velocity of any point in the shell. The supports were constrained in all translations and rotations. The loading pins were modelled as rigid hollow cylinders made of shell elements, allowed to translate only along the vertical axis. An implicit time integration method was chosen, hence eluding all possible dynamic effects. It was convenient to extract rigid body displacement of loading pins and resultant interface force between specimen and rigid loading pins, to compare with the experimental force-displacement graph.

## 4.4 Optimization set up in LS-OPT

### 4.4.1 Introduction

Optimization was carried out in LS-OPT, to find the optimal value of the model parameters that would replicate the material behaviour extracted during testing. The material parameter identification process was distinguished as regular routine and FFC routine, depending on the target data. In the regular routine, the target data is the curve seen in [Figure 10a](#), implying that the objective of the optimization is to achieve similar force-extensometer strain response. For FFC routine, the target data is a family of curves as seen in [Figure 10b](#), implying that the objective of the optimization is to achieve identical strain fields. As it can be seen in the [Table 1](#), there are a total of 10 model parameters. Due to the large number of model parameters, the optimization was split into two stages. A Hardening stage deals with the optimization of the simulation response to match with the material behaviour until necking point. Meanwhile, a Damage and failure stage deals with the same after the necking point.

The Successive Response Surface Method (SRSM) with an adaptive domain reduction is employed because of its robustness, computational efficiency and rapid convergence to the region of optimum. More details, regarding the theoretical description of adaptive domain reduction implemented in LS-OPT, are covered in the work by [Stander and Craig \(2002\)](#). Quadratic response surfaces are constructed in a sub region of design space using a D-optimal experimental design for point selection with a design of experiments approach. A starting value and a bound was provided for each model parameter.

#### 4.4.2 Regular routine

The setup of the optimization problem in LS-OPT is as shown in [Figure 15](#). The stage Yield\_curve deals with an execution of a python file. The python file contains a script which processes the yield curve and produces an include file. The results from the Yield\_curve stage are set to be automatically transferred to Simulation stage directory. To extract a response similar to the extensometer true strain, an expression is used which contains the nodal displacements of the two nodes constituting extreme ends of an extensometer. With the help of another expression, the true strain is calculated through extensometer displacement. A crossplot of force vs. extensometer true strain is generated using the built-in crossplot feature. The DTW algorithm is used to match two histories and measure the similarity between them. Since the DTW similarity measure is highly sensitive to noise, the comparison between correct part of the curves can be achieved through the usage of lookup function under responses tab. The optimization was carried out with a single objective of minimizing the curve matching error. For the Damage and failure stage, the optimal model parameters obtained during the Hardening stage were considered as constants. For the Damage and failure stage, MSE method was used to compare the curves.

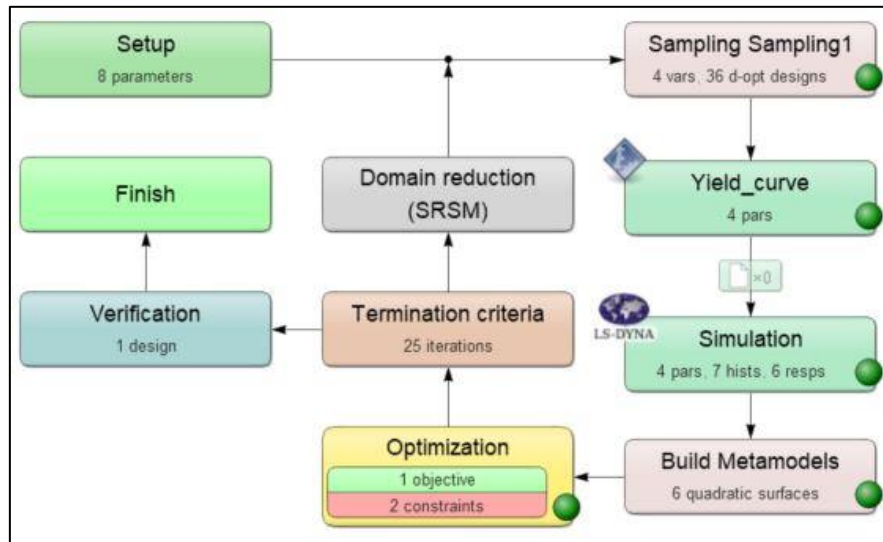


Figure 15 Optimization setup in LS-OPT

### 4.4.3 FFC routine

The FFC routine also follows the same workflow as discussed in the previous section, but with change of history to multi-point history. Because of the difference in test point coordinates obtained during the experiment and the coordinate system of the simulation model, there is a need to align test point set to the FE nodes. This is achieved by a built-in alignment option (see Figure 16) that uses least square formulation to transform the test point set so that it aligns with the FE nodes. It is not a necessary condition that the test points should spatially coincide with the FE nodes. The LS-OPT algorithm allows a 3D one-to-one mapping of test points onto the nodes or elements using a binary tree. This is done through the nearest nodal neighbour algorithm (Stander, Basudhar et al. July 2019). An alternative to this is an ability of the LS-OPT algorithm to interpolate fields within each element. The alignment of test point set with the FE nodes at the region of interest can be seen in Figure 17.

Transformation Name					
alignment					
Source			Simulation		
Coordinates			Coordinates		
Test x coord	Test y coord	Test z coord	Sim x coord	Sim y coord	Sim z coord
-0.00764548	-15.6117	0.0357078	5.05	47.6	2
8.26151	57.9462	0.2056	14.2	121.6	2
8.33334	-14.6871	-0.134184	14.78	48.1	2

Figure 16 A user interface for alignment of test set cloud to FE nodes in LS-OPT

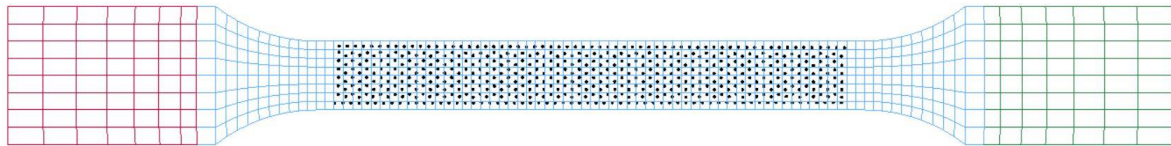


Figure 17 Alignment of test point set with the FE nodes

For the multi-point history response, the upper surface yy-strain under multihistories tab was chosen and a crossplot of force and U\_surf\_yy\_strain was set up to compare with the ARAMIS input.

## 4.5 Element size regularization

It was previously discussed in section 3.1.2 about the spurious mesh dependency of calibrated GISSMO parameters. The possibility of compensating for the change in element size, through a load curve defining a scale factor for equivalent plastic strain to failure against the corresponding element size, is explored. Another possibility for compensating the element size changes is through a load curve defining the element-size dependent fading exponent. In this thesis, the focus will be only on the former. FE models of different mesh sizes are generated and an optimization is carried out for each model to find out the value of equivalent plastic strain to failure that adjusts the softening part of the curve to match with the target data. For a solid element, its size is given by the

cube root of its volume. Scale factor is the ratio of equivalent plastic strain to failure values for the mesh under consideration to that of the original mesh.

## 4.6 Comparisons

The calibrated material models will then be compared with the data extracted from the same tensile test but with different gauge lengths of the extensometer. The force vs. true strain data was extracted from an experiment, for 50 mm and 25 mm gauge length extensometers (see [Figure 18](#)). A similar strategy as before will be adopted to obtain corresponding extensometer true strain from the simulation, for both gauge lengths.

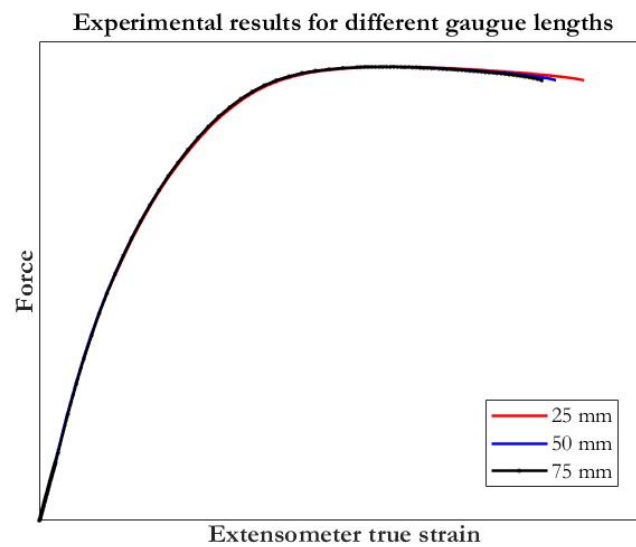


Figure 18 Experimental force vs. extensometer true strain for 75 mm, 50 mm and 25 mm gauge lengths



# 5. Results

## 5.1 Regular vs. FFC routine

A comparison between the target curve and the calibrated response for the two different routines can be seen in Figure 19. It is worth noting that for the regular method, the experimental and the simulated force vs. extensometer true strain curves are in close agreement. In Figure 19b, a non-uniformity in the strain field present in the experimental data, even before the point of necking, is to be observed.

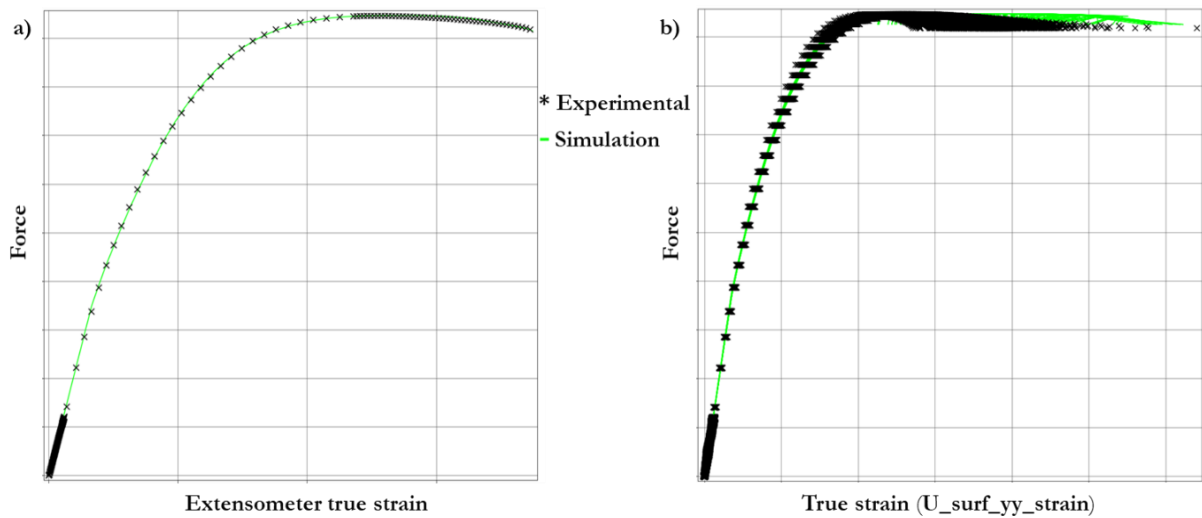


Figure 19 Comparison between the target data and the calibrated response for a) Regular routine and b) FFC routine

A similar multi-point history, including only the hardening part, with the introduction of geometric perturbation of nodes through the keyword \*PERTURBATION\_NODE, can be seen in Figure 20a. The optimal parameters obtained from the FFC routine were used in this simulation which produced a harmonic perturbation of nodes along the length of the specimen. The resulting stochastic distribution of strain field along with its experimental counterpart is shown in Figure 20b. A contour plot of y-strain is adopted for all the comparisons in this section.

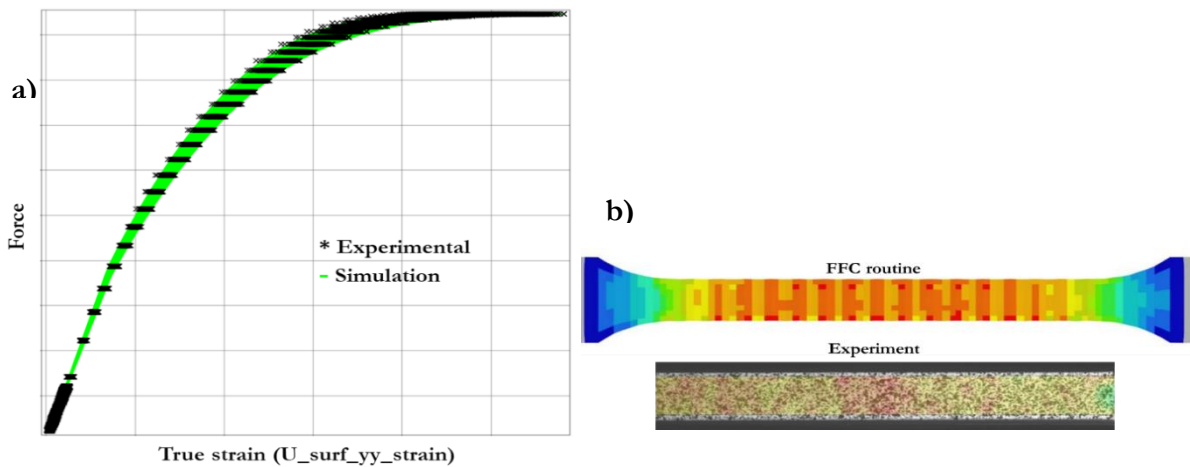


Figure 20 A comparison of the response and the y-strain contour plot attained after the introduction of nodal perturbations with the experimental counterpart



A comparison among the strain fields (just before the specimen breaks), obtained through the calibrations and the experiment, is carried out (see Figure 21). It can be observed that the localization is more pronounced in the specimen that underwent the regular routine. The similarity in the strain-contour plots obtained from the FFC routine and the experiment indicates that the specimen does not undergo a pronounced localization.

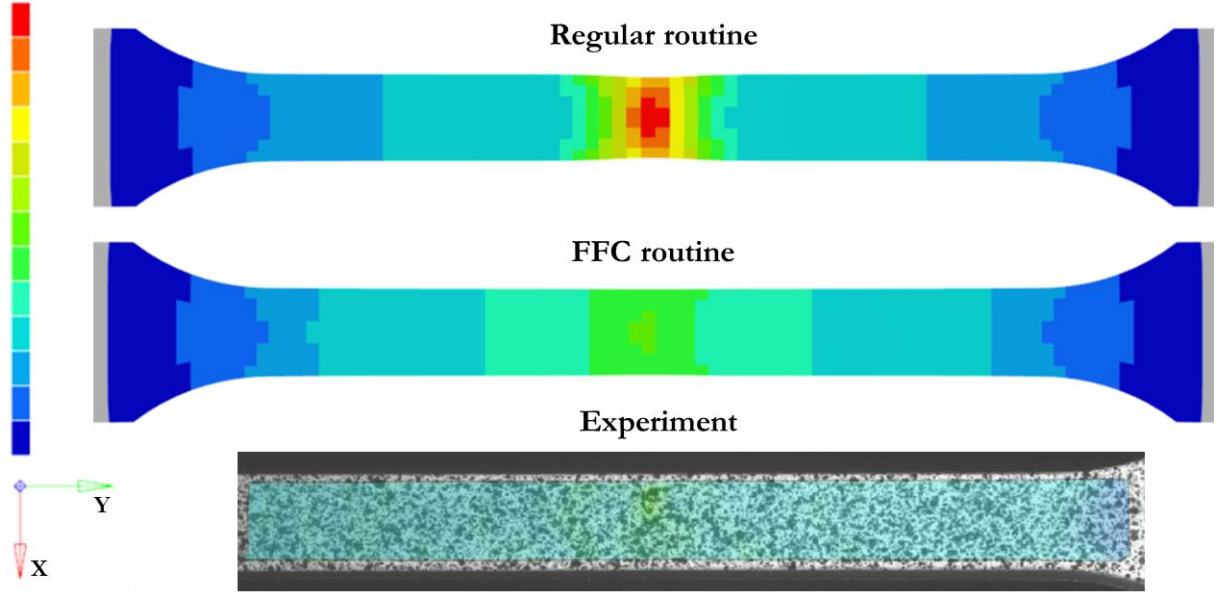


Figure 21 A comparison among the y-strain contour plots obtained from regular routine, FFC routine and the experiment

The strain-contour plot from the regular routine is removed to achieve a more accurate comparison between the FFC routine and the experiment (see Figure 22). The tiny red patch in the lower specimen indicates the small amount of localization that occurred at that position, just before the breakage. But, in the upper specimen, the localization is dispersed around the centre point of the specimen. The point at the extreme right of the graph (see Figure 19b) corresponds to the value of strain data extracted from the facet point present close to the red patch.

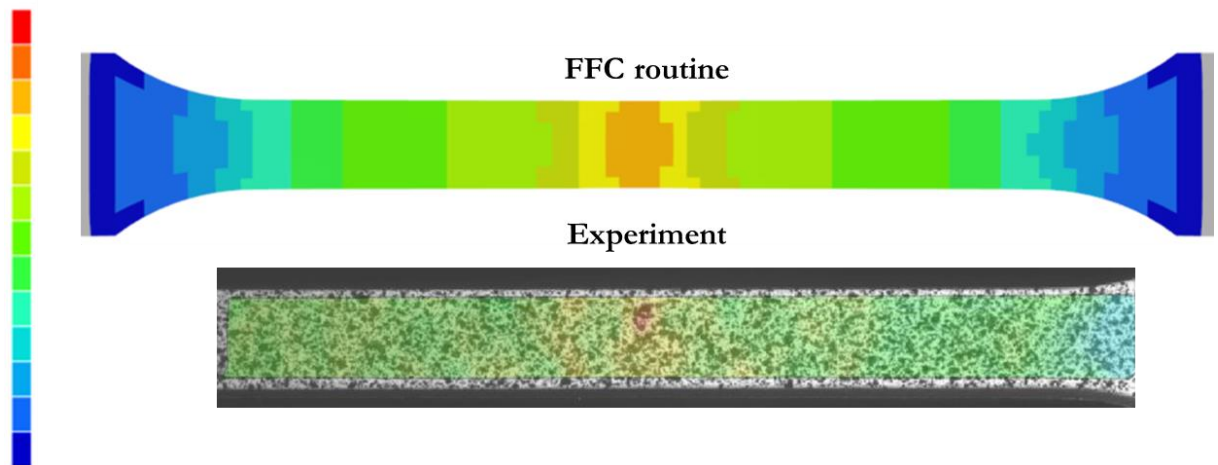


Figure 22 A comparison between the strain-contour plots obtained from the FFC routine and the experiment

The optimal value of model parameters, obtained for each routine, is compared in Table 2. The optimal values are normalised against the corresponding values obtained from FFC routine. The model parameters that were optimised during the Hardening stage have their values very close between the two routines. The maximum percentage difference being just over 5% for the first set of model parameters. For the model parameters that were optimised under Damage and failure stage, there are higher percentages of the differences, as it was also seen in the difference in strain-contour plots. The equivalent plastic strain, that each element has to undergo before it fails, is approximately 80 % higher for the regular routine than the FFC routine.

Stage	Parameters	FFC routine	Regular routine	% difference <sup>§§</sup>
<b>Hardening</b>	Young's modulus	1	1	0
	A	1	1	0
	B	1	0.947	-5.3
	C	1	1.011	1.1
	N	1	1	0
<b>Damage and failure</b>	FADEXP	1	2.859	185.9
	DMGEXP	1	0.966	-3.4
	ECRIT	1	1.024	2.4
	Y_LCSDG	1	1.799	79.9
	Slope at point B	1	1.637	63.7

Table 2 A comparison between the optimal values of model parameters obtained for the regular and the FFC routine

## 5.2 Comparisons with different extensometer gauge lengths

After the material models were calibrated against the corresponding target curves, the validation of the material model had to be carried out. Considering the 75 mm extensometer measurements as

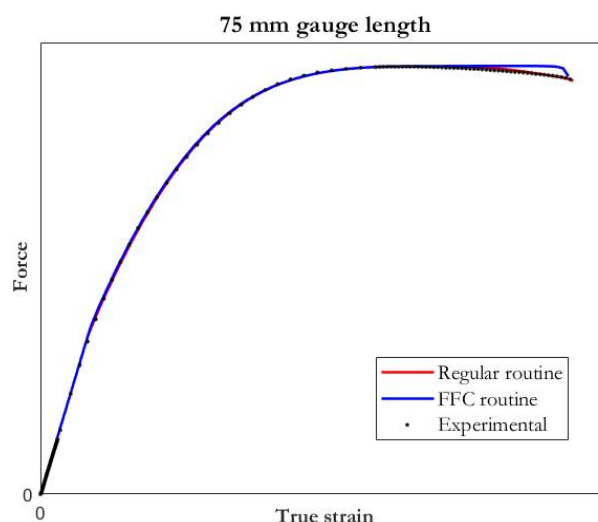


Figure 23 Comparisons among the Experiment, FFC and regular routines with 75 mm gauge length extensometer

<sup>§§</sup> (Regular-FFC) ×100 and rounded off to one decimal.

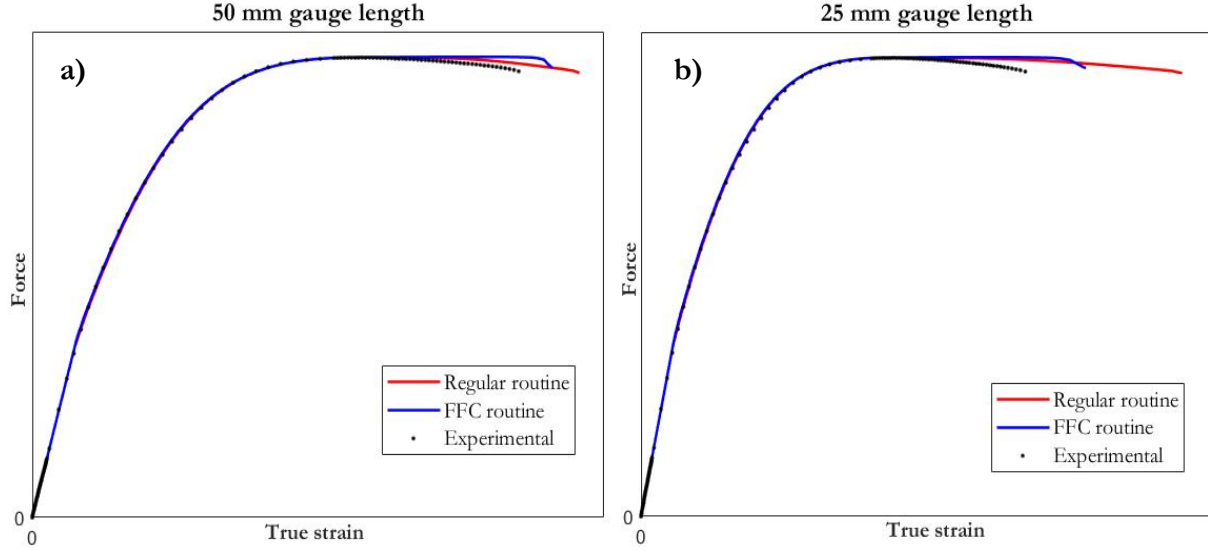


Figure 24 Comparisons among the Experiment, FFC and regular routines with a) 50 mm gauge length and b) 25 mm gauge length extensometer

the global measurements, more local comparisons had to be carried out to study the merits of the FFC routine. For this reason, two different extensometers of gauge length 50 mm and 25 mm were employed to measure more local extensometer strains. For the 75 mm gauge length extensometer, it can be seen in Figure 23 that the force vs. true strain curves are in a fairly good match. For the 50 mm gauge length extensometer (see Figure 24a), the true strain at failure has increased for both the calibrated material models. The same trend follows for the 25 mm gauge length extensometer (see Figure 24b). In fact, the difference in true strain obtained through the regular and FFC routine models increases as it measures more locally.

### 5.3 Element size regularization

The element size regularization was carried out with 4 different mesh sizes in addition to the original mesh size used. The element-size dependent regularization curves for each of the routines can

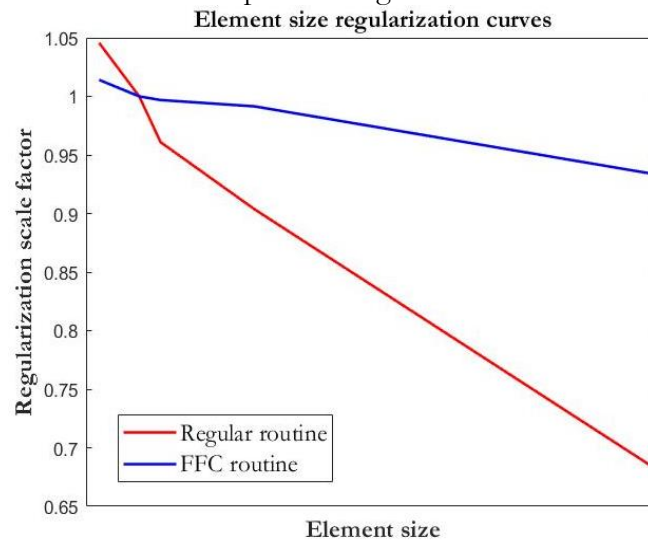


Figure 25 Element size regularization curves for the two routines

be seen in Figure 25. For the element sizes outside the range, LS-DYNA linearly extrapolates the curve to the required element size. The equivalent plastic strain to failure increases as the element size decreases and vice-versa. The variation of regularization scale factor over the element size is low in case of full-field calibrated model compared to its regular counterpart.

## 5.4 Three-point bending

Force and displacement were extracted from the loading pin and a relation between the two quantities, in the form of a graph is constructed. A comparison is made among the experiment and the two different routines, which is depicted in Figure 26. It can be observed that in the specimen from regular routine, the elements do not fail at all. But, a fracture does occur in the other two specimens. The loading pin displacement at the moment of fracture, for experimental and FFC routine model, is comparable. It is to be noted that the calibrated models are exhibiting stiffer behaviour than in the experiment. The difference can be quantified, in the region of linear elasticity, with the help of the equations derived in section 3.3. In the linear elastic region, for a given displacement, the calibrated material models and the analytical equation yield the values of force within 9 % difference with each other. In the experiment, the specimen shows 30 % softer behaviour compared with the calibrated models.

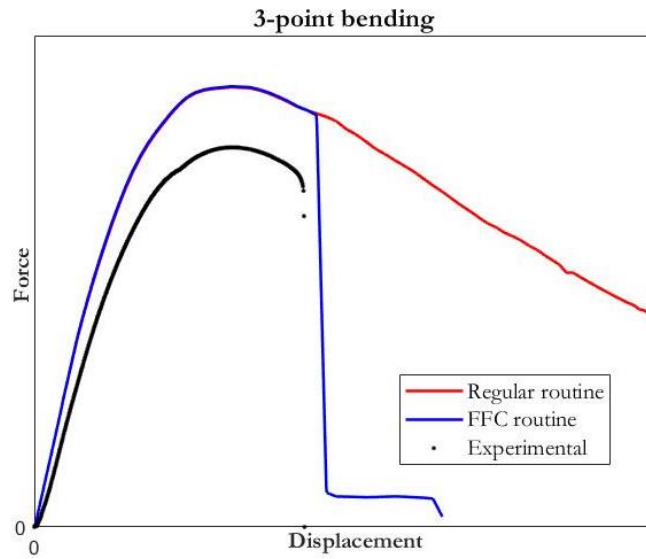


Figure 26 Comparisons among the Experiment, FFC and regular routines with a 3-point bending test

## 5.5 Four-point bending

Similar comparisons, as in the previous section, are to be carried out among the force vs. displacement curves (see Figure 27). It can be noticed that there is a difference between the experimental curve and the curves from calibrated material models. The difference in the linear elastic regime of the material behavior can be quantified using the analytical equations described in section 3.4. It is observed that the difference between the forces obtained for the calibrated models and the analytical solution, for a given displacement, is approximately within 13 %. The difference, considering

the same as above, between the experiment and the calibrated model is calculated to be approximately 17 %.

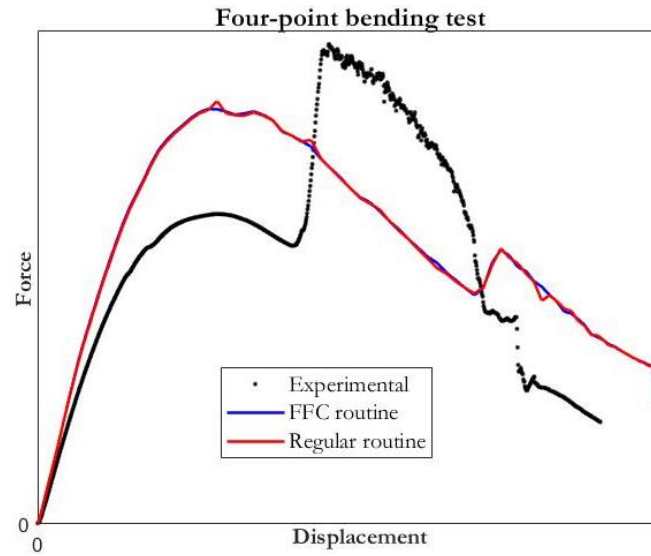


Figure 27 Comparisons among the Experiment, FFC and regular routines with a four-point bending test

It is also seen that even for the higher values of loading pin displacement, the calibrated material models do not exhibit failure. Also, the curves from the FFC routine and the regular routine describe a similar behavior despite showing differences in the previous comparisons. A detailed study on both the simulated models were carried out and a fringe plot of the effective plastic strain for the full-field calibrated model is presented in [Figure 28](#).

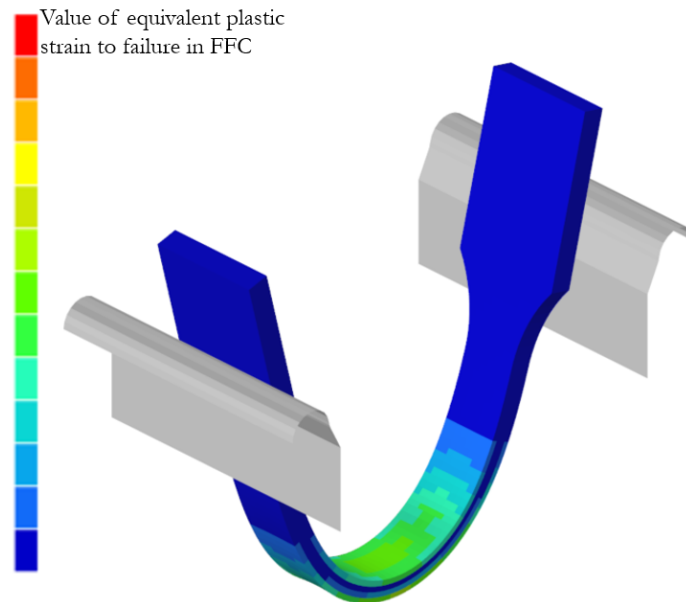


Figure 28 A contour plot of effective plastic strain at the highest displacement of loading pins

The legend is set in such a way that the color red represents the value of equivalent plastic strain to failure ( $Y_{LCSDG}$ ) of the full-field calibrated model. It can be seen that the plastic strain in the elements is not as high for the failure to occur. As the loading pins move vertically and deform the specimen model, the deformation occurs to an extent and then the specimen model starts to slide

down the supports. The value of maximum effective plastic strain, seen in the contour plot of the deformed specimen in [Figure 28](#), is indicated with the help of an arrow in [Figure 29](#). [Figure 29](#) is a comparison between yield curves obtained for each of the routines.

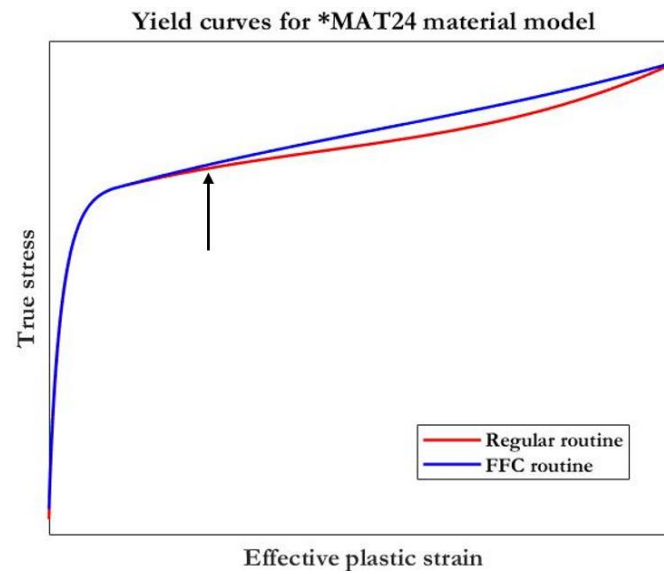


Figure 29 Yield curves obtained from calibrations

## 6. Discussion

The impact of localization in the measurement of strain across different gauge lengths, was acknowledged through the behavior of curves observed in [Figure 18](#). The observation further emphasized the need for extracting data from the localization zone. A full-field calibration of the material model was carried out against the multi-point history data which was extracted during the experiment with the help of Digital Image Correlation technique. To compare and contrast, a conventional way of calibrating the material model against the extensometer data was adopted. It was observed, despite a very close match between the target and response curves (see [Figure 19a](#)), the material model calibrated through the regular routine shows a ductile behavior. The observation was supported by the strain-contour plots (see [Figure 21](#)). The ductile behavior of the elements is answered by the value of equivalent plastic strain to failure obtained from the regular routine. The objective of the optimization was only to fit the global data and the event occurring in the middle was not taken into account. On the other hand, the material model calibrated through the FFC routine shows a comparatively low localization and hence a lesser ductile behavior. But, as seen in the experiment, the specimen exhibits a very brittle behavior with a slight reduction of force before failure. During the optimization in the FFC routine, it was experienced by the author that there was a trade-off between the reduction of force and the value of equivalent plastic strain to failure. If the force value, post the necking point, has to be reduced to what it is in the experiment, then the specimen has to undergo a localization which will lead to higher equivalent plastic strain to failure. A higher value of equivalent plastic strain to failure implies that the specimen will no longer undergo a brittle failure. A balance (see [Figure 19b](#)) had to be brought in between both the quantities manually. In addition to this, the resulting model should be able to predict the correct (as in the experiment) extensometer displacement at failure, which implicitly depends on the damage parameters. A combination of all these had to be taken care of during the optimization which demanded a substantial human supervision. According to the author, the key to an easier optimization is to narrow down the design space through manual design of experiments.

The non-uniform strain behavior before the necking point was seen in the simulation response through the introduction of geometric non-linearity. The amplitude of the harmonic perturbation used in the simulation model is high and does not exist in that magnitude in the real specimen. This would lead to a possibility that the non-uniform strain field before the necking point might be because of a material inhomogeneity. The claim can be supported by the fact that the specimen is manufactured through injection molding and consists of 30% glass fiber reinforcement. The orientation and the distribution of glass fibers play a major role in specimen behavior. The manufacturing process plays a major role as the factors such as mold surface, flow conditions involve in governing the fiber orientation. For short-fiber reinforced plastics manufactured from injection molding, the fibers in the boundary layers are orientated in the filling direction and the ones in the core layer are oriented perpendicular to the filling direction. More details can be found in the work of [Müller, Brylka et al. \(2016\)](#). But in contrast to the aforementioned study, the specimen, in this case, shows a softer behavior in bending than in tension. A detailed study, right from the manufacturing of the specimens, needs to be carried out to answer several discrepancies observed in the material behavior. Another aspect that cannot be neglected is a possible error in measurement. This hypothesis gathers more support because of the presence of non-uniformity in the strain field of



the homogenous PA6 material (see [Appendix 3: A short study on PA6 Material](#)). A similar non-uniformity in strain field, as previously seen in glass fiber reinforced PA6 material, can also be observed in the y-strain contour plot of PA6 specimen (see [Figure 34c](#)).

The gain of implementing FFC routine over regular routine can be witnessed through [Figure 24](#). Also, [Table 2](#) presents the value of equivalent plastic strain to failure for each of the routines. The elements in the model from the regular routine undergo approximately 80 % higher strain than their counterparts from the FFC routine. Meaning, if the material model from regular routine is used in a simulation of a component, then the component would exhibit a ductile behavior leading to an inaccurate prediction. The time taken for calibration through regular and FFC routines are four and two weeks, respectively. Also, it needs to be noted that the time taken for calibration will significantly depend on the competence of the individual performing the task. In the course of calibration through the regular routine, the author had gained competence and experience and thus the calibration through FFC routine took comparatively less time. According to the author, calibration through both the routines demand similar amount of time. Hence, with similar amount of calibration time required, the FFC routine has an advantage of more accurate material behavior prediction over the regular routine. Since the damage model GISSMO is capable to account for the stress-state dependent failure, more number of tests can be carried out to calibrate the material model so that it could account for a wide range of triaxialities.

The validations of the calibrated material models were carried out through their implementation in three-point and four-point bending tests. A major assumption underlying the simulations is that the tension-compression asymmetry is neglected. The material model behaves identically in both tensile and compressive loadings. A plausible explanation to the softer behavior of the specimen in bending might be because of the spatial distribution or orientation of the glass fibers reinforced with the binding material. One can expect the difference between analytical and simulation response, in the linear elastic regime, as the analytical equations are formulated based on the assumptions from the beam theory ([Hopkins, Patnaik et al. 2003](#)). Also, the values of frictions in the contact definitions are assumed by the author. In case of the comparisons among the force-displacement curves of four-point bending, one can notice that the curves from the FFC and the regular routines are in close agreement to each other in spite of their difference in previous comparisons. The identical force-displacement behavior can be explained with the help of yield curves present in [Figure 29](#). The magnitude of maximum effective plastic strain in the specimen in [Figure 28](#) is indicated in [Figure 29](#) by the arrow. One can notice that both the curves are in close agreement to each other around that region and hence identical behavior can be expected.



## 7. Conclusion and future work

### 7.1 Conclusions

A comparison in strain fields, obtained from the experiment and the two different routines, shows that the regular routine is only able to accurately mimic the global behaviour of the specimen. On the other hand, the FFC routine takes into account both the global behaviour and the strain field in the specimen and therefore predicts the material behaviour better than the regular routine. The gain of accuracy in prediction of material behaviour, achieved through FFC routine over the regular routine, was further backed up through different comparisons and validations. The gain in accuracy was not significant until the point of necking in the material behaviour. Hence it is recommended by the author, to use the equations (3) and (7) to set up the yield curve until the necking point for uniaxial tests. Demanding similar amount of calibration time in Damage and failure stage, the FFC routine has an advantage of more accurate prediction of material behaviour over the regular routine.

### 7.2 Future work

A possible future work would be to conduct a detailed study to find the cause for non-uniform strain field before necking point. The study can be carried out on the material characteristics and measurement of strains in ARAMIS. It must also be confirmed if the non-uniform strain field before necking point is due to an error in measurement or an error in implementation of DIC technique. It can be done through an experiment on a metallic specimen as the implementation of DIC in characterization of metals has been carried out by many. It can be seen through the works of Ilg, Haufe et al. (2018) that there is a uniform strain field until necking point in metals. A detailed study on glass fibre distribution and orientation during the injection moulding process of the specimen would reveal the material characteristics that yield softer behaviour in bending. In this thesis, the material model is calibrated only for a single load case and hence there is a possibility to carry out a similar work for a variety of load cases to build a complete material card for the damage model.

# References

1. (2012). International Standard. ISO 527-2, Plastics — Determination of tensile properties — Part 2: Test conditions for moulding and extrusion plastics—Test report, ISO.
2. Andrade, F., M. Feucht and A. Haufe (2014). On the prediction of material failure in LS-DYNA: A comparison between GISSMO and DIEM.
3. Björk, K. (2007). Formler och tabeller för mekanisk konstruktion : mekanik och hållfasthetslära, Karl Björks förlag.
4. Bridgman, P. W. (1952). Studies in Large Plastic Flow and Fracture: With Special Emphasis on the Effects of Hydrostatic Pressure. United States of America, McGRAW-HILL BOOK COMPANY, INC.
5. Effelsberg, J., A. Haufe, M. Feucht, F. Neukamm and P. DuBois (2012). On Parameter Identification for the GISSMO Damage Model. 12<sup>th</sup> International LS-DYNA Users Conference. Detroit.
6. GOM (2016). 3D Testing- Technical Documentation- Digital Image Correlation and Strain Computation Basics, GOM GmbH.
7. Hallquist, J. O. (2006). Belytschko-Lin-Tsay shell. LS-DYNA Theory manual, Livermore Software Technology Corporation.
8. Hallquist, J. O. (2006). Material model: Piecewise linear isotropic plasticity. LS-DYNA Theory manual, Livermore Software Technology Corporation.
9. Hockett, J. and O. Sherby (1975). "Large strain deformation of polycrystalline metals at low homologous temperatures." Journal of the Mechanics and Physics of Solids **23**(2): 87-98.
10. Hopkins, D., S. Patnaik and D. Hopkins (2003). Displacement in a Beam. Strength of Materials : A New Unified Theory for the 21st Century. Burlington, UNITED STATES, Elsevier Science & Technology: 164-178.
11. Hopkins, D., S. Patnaik and D. Hopkins (2003). Flexure Formula. Strength of Materials : A New Unified Theory for the 21st Century. Burlington, UNITED STATES, Elsevier Science & Technology: 153-158.
12. Ilg, C., A. Haufe, D. Koch, N. Stander, K. Witowski, Å. Svedin and M. Liewald (2018). Application of a Full-Field Calibration Concept for Parameter Identification of HS-Steel with LS-OPT®.
13. Khan, A. S. and S. Huang (1995). Yield criteria. Continuum theory of plasticity, Wiley: 94-104.
14. Lemaitre, J. (1985). "A Continuous Damage Mechanics Model for Ductile Fracture." Journal of Engineering Materials and Technology **107**: 83-89.
15. LSTC (2017). \*MAT\_RIGID. LS-DYNA®: Keyword User's Manual. **2**.
16. Müller, V., B. Brylka, F. Dillenberger, R. Glöckner, S. Kolling and T. Böhlke (2016). "Homogenization of elastic properties of short-fiber reinforced composites based on measured microstructure data." Journal of Composite Materials **50**(3): 297-312.
17. Myers, R. H., D. C. Montgomery and C. M. Anderson-Cook (2016). Estimation of the Parameters in Linear Regression Models. Response surface methodology : process and product optimization using designed experiments, Wiley: 14-21.

18. Myers, R. H., D. C. Montgomery and C. M. Anderson-Cook (2016). Response Surface Methodology. Response surface methodology : process and product optimization using designed experiments, Wiley: 1-2.
19. Neukamm, F., M. Feucht and A. D. Haufe (2009). Considering damage history in crashworthiness simulations. 7<sup>th</sup> European LS-DYNA Conference. Salzburg, DYNAmore GmbH.
20. Roux, W. J., N. Stander and R. T. Haftka (1998). "Response Surface Approximations For Structural Optimization." International Journal For Numerical Methods in Engineering **42**: 517-534.
21. Spencer, A. J. M. (2004). The Deformation gradient tensor. Continuum Mechanics, Dover Publications: 68-70.
22. Stander, N., A. Basudhar, W. Roux, K. Witowski, T. Eggleston, T. Goel and K. Craig (July 2019). Full-field material calibration. LS-OPT® User's Manual, Livermore Software Technology Corporation: 625-631.
23. Stander, N., A. Basudhar, W. Roux, K. Witowski, T. Eggleston, T. Goel and K. Craig (July 2019). Normalized Dynamic Time Warping. LS-OPT® User's Manual, Livermore Software Technology Corporation: 620-622.
24. Stander, N., A. Basudhar, W. Roux, K. Witowski, T. Eggleston, T. Goel and K. Craig (July 2019). Ordinate-based Curve Matching. LS-OPT® User's Manual, Livermore Software Technology Corporation: 617-618.
25. Stander, N. and K. J. Craig (2002). "On the robustness of a simple domain reduction scheme for simulation-based optimization." Engineering Computations **19**(4): 431-450.
26. Stander, N., K. Witowski, C. Ilg, A. Haufe, M. Helbig and D. Koch (2018). Application of Digital Image Correlation to Material Parameter Identification. Advances in Structural and Multidisciplinary Optimization, Cham, Springer International Publishing.
27. Weck, A., D. S. Wilkinson, H. Toda and E. Maire (2006). "2D and 3D Visualization of Ductile Fracture." Advanced Engineering Materials **8**(6): 469-472.

## Appendix 1: Example: DTW

A general and rather simple example of how a Dynamic Time Warping algorithm calculates the similarity between two curves B and C having data points written in the vector form as  $B = (10, 30, 15, 5, 25)$  and  $C = (5, 30, 10, 25, 30)$  is illustrated below. Only one-dimensional Euclidean distance is considered in this example. The data points can be represented with the help of indices  $i$  and  $j$  as  $B_i$  and  $C_j$ , such that  $i = 1, 2, \dots, 5$  and  $j = 1, 2, \dots, 5$ . A matrix of accumulated distance, of order  $i \times j$ , can be written as shown in the figure below.

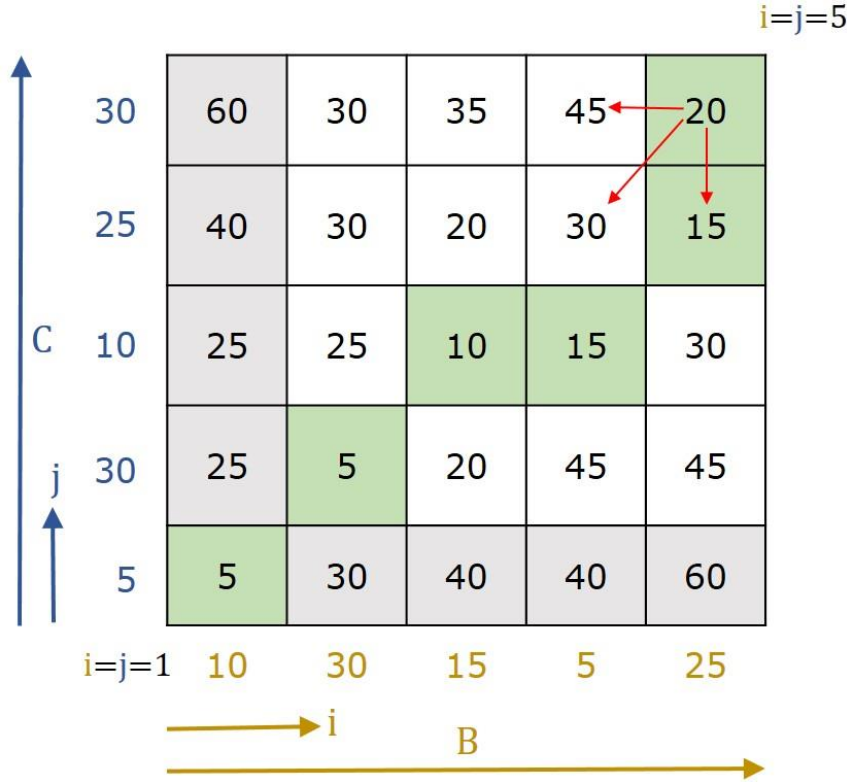


Figure 30 Accumulated distance matrix to calculate minimum warping path

The accumulated distance matrix,  $ACCDIST(i, j)$  can be formulated as follows,

- For  $i = 1$  and  $j = 1$ ,  $ACCDIST(i, j) = |B_i - C_j|$ ;
- For  $i = 1$  and  $2 \leq j \leq 5$ ,  $ACCDIST(i, j) = |B_i - C_j| + ACCDIST(i, j - 1)$ ;
- For  $j = 1$  and  $2 \leq i \leq 5$ ,  $ACCDIST(i, j) = |B_i - C_j| + ACCDIST(i - 1, j)$ ;
- For  $2 \leq i \leq 5$  and  $2 \leq j \leq 5$ ,

$$ACCDIST(i, j) = |B_i - C_j| + \min \begin{cases} ACCDIST(i - 1, j) \\ ACCDIST(i - 1, j - 1) \\ ACCDIST(i, j - 1) \end{cases}.$$

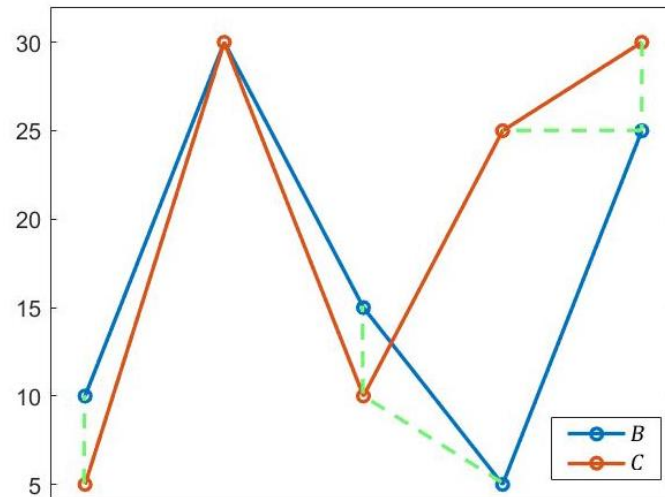


Figure 31 DTW matching of the points between two curves

The warping path can be found, starting from the point  $(i, j) = (5, 5)$ , by choosing a path that accumulates the least distance. The warping path gives an idea of the similarity between polygons B and C. This is a rather simplified example of the originally formulated algorithm<sup>\*\*\*†††</sup>. The green dotted lines, in Figure 31, shows that DTW allows one-to-many matchings.

---

<sup>\*\*\*</sup> Souza, C., C. Pantoja and F. C. Souza (2009). Verificação De Assinaturas Offline Utilizando Dynamic Time Warping. Anais do IX Congresso Brasileiro de Redes Neurais, Sociedade Brasileira de Redes Neurais: 1-5.

<sup>†††</sup> Poli, G., J. F. Mari, J. H. Saito and A. L. M. Levada (2007). Voice Command Recognition with Dynamic Time Warping (DTW) using Graphics Processing Units (GPU) with Compute Unified Device Architecture (CUDA). 19th International Symposium on Computer Architecture and High Performance Computing (SBAC-PAD'07).

## Appendix 2: Generic specimen from bending tests

As discussed before, five specimens were considered for each test. A specimen which exhibits a mean valued behavior was considered further in the calibration process. The data from all the specimens that underwent three-point (see [Figure 32](#)) and four-point (see [Figure 33](#)) bending tests, along with their average or mean value can be seen below.

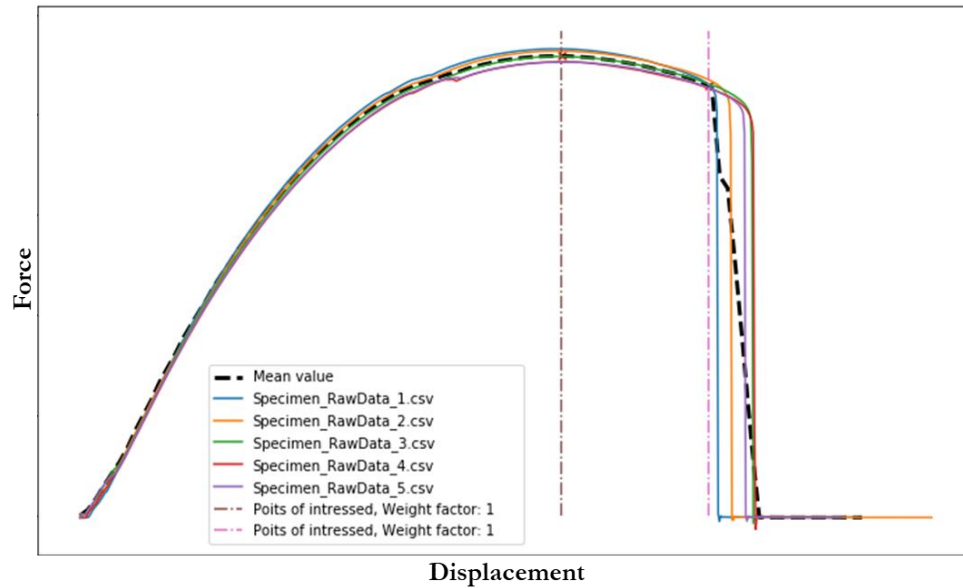


Figure 32 Data extracted from three-point bending tests

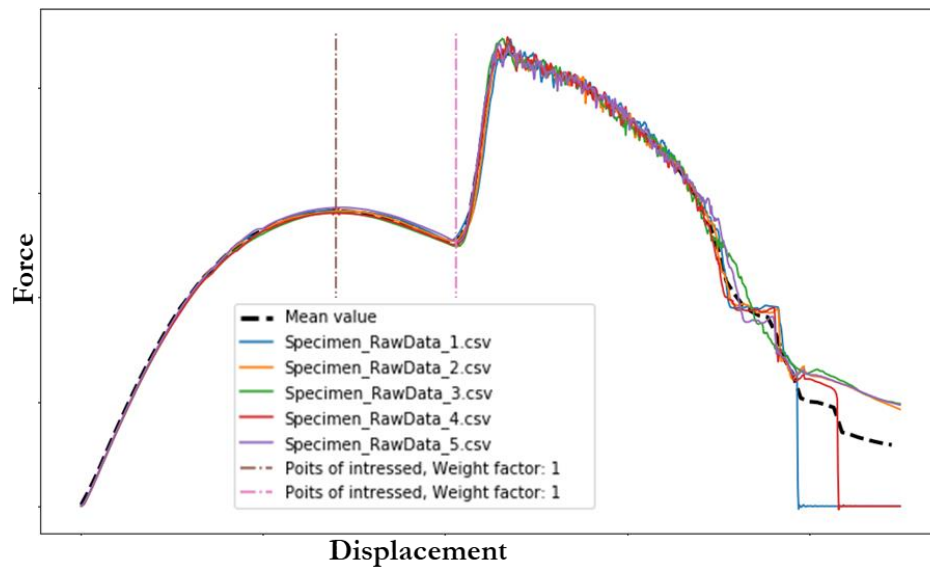


Figure 33 Data extracted from four-point bending tests

## Appendix 3: A short study on PA6 Material

A short study on behavior of the homogenous PA6 (Polyamide 6) material was carried out with an existing data that was available at the author's disposal. The data was extracted from a tensile test carried out at 50 millimeters per minute velocity, same velocity as the tests carried out before, ensuring the quasi-static condition. The output from the ARAMIS is presented below.

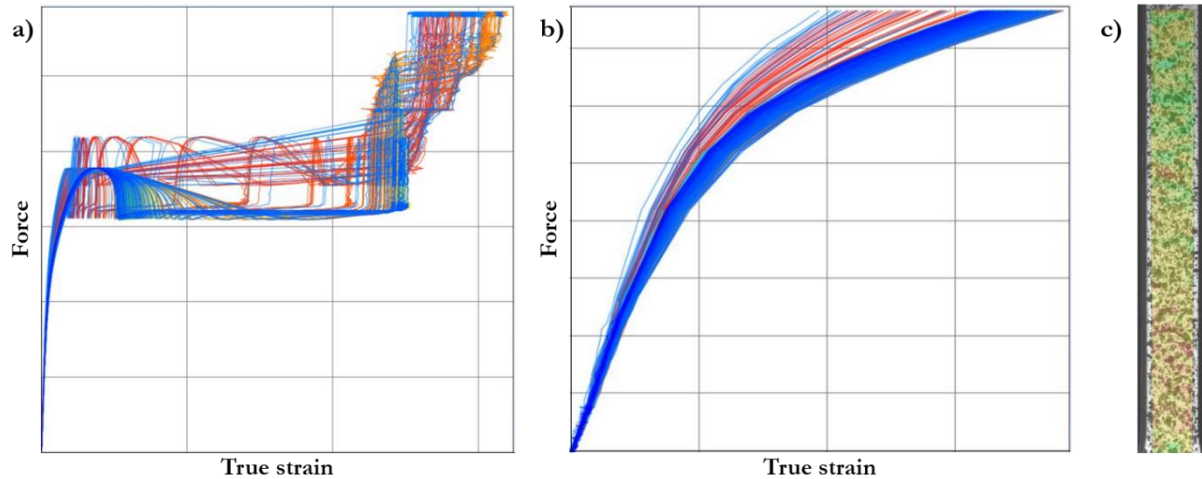


Figure 34 a) Force vs. True strain for 75 mm gauge length region b) Hardening part of the curve for 75 mm gauge length region c) True strain contour plot of the specimen's surface

A closer look at [Figure 34a](#) reveals that a number of lines vanish in the mid-way as the deformation takes place. This is because the facet points move out of the camera frame. This can be expected as PA6 is a very ductile material. Even though the tensile specimen is made up of a homogenous material, there is a spread in true strain curves (see [Figure 34b](#)) before the force reaches its first maximum value. A contour plot of true strain on the specimen surface (see [Figure 34c](#)) also hints the non-uniformity of the strain field. The behavior becomes less apparent in a plot (for example in [Figure 34a](#)) as the magnitude of true strain at failure increases.

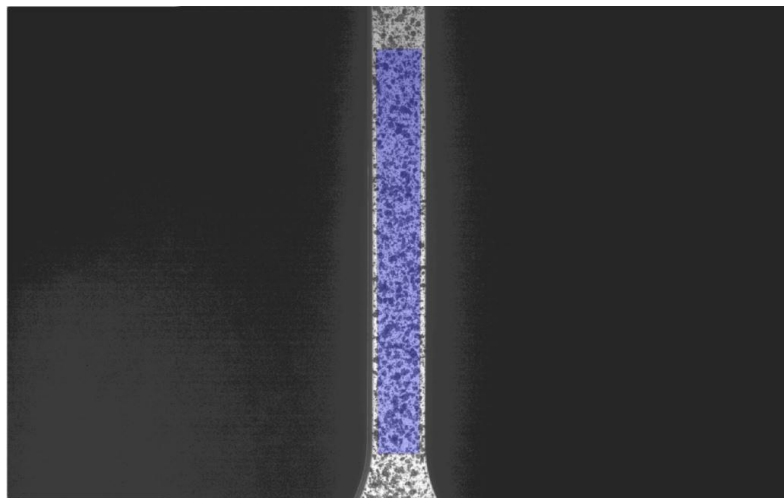


Figure 35 An initial calibration image from ARAMIS

The initial calibration image for the current tensile test can be seen in [Figure 35](#). To prevent the loss of data resulting from the facet points moving out of the camera frame, the author suggests following measures. The camera could be rotated 90 degrees so that the longer edge of the image is aligned along the length of the specimen. Although expensive, there is an advantage if the geometry of the specimen can be changed. As smaller specimens undergo less deformation before failure, increasing the chance that the facet points will remain within the frame.

Instead of the entire region along the gauge length, a smaller region (see [Figure 36b](#)) where the necking occurs can be considered for the extraction of true strain data. The force vs. true strain output from the ARAMIS is presented in [Figure 36a](#). Later with the help of alignment option in LS-OPT, the point cloud can be aligned to the nodes at the central region of the specimen. This has to be done as the failure in a FE model of the specimen is bound take place around the central region.

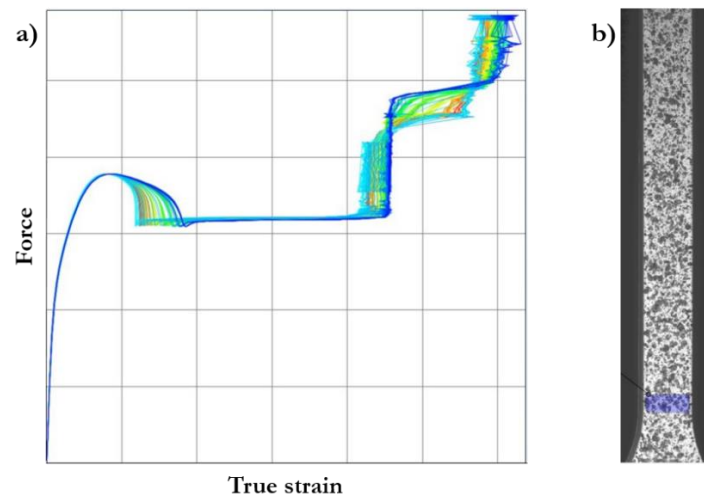


Figure 36 a) Force vs. True strain for a small region highlighted in b)

A calibration was attempted with the available data of force vs. grip displacement and the output curve is plotted against the experimental curve as shown in [Figure 37a](#). The grip displacement during the failure of the specimen is around 320 mm, suggesting the ductility of the thermoplastic material.

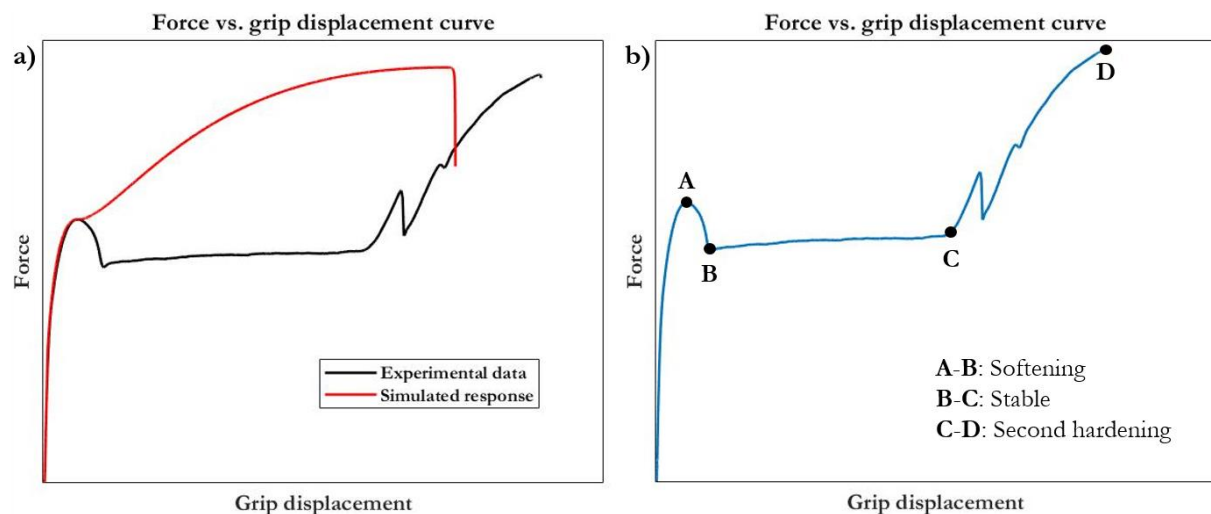


Figure 37 Force vs. grip displacement curve b) and comparison with simulation response a)



For the ease of explanation, the graph of force vs. grip displacement, after the necking point, is divided into three parts (see [Figure 37b](#)). According to the author, the initial softening after the necking point can be achieved with the help of GISSMO damage model. But the element fails as it softens and the steady part of the curve is hard to obtain. There is a need to overcome the inability of the element to harden after it is softened. It must also be noted that the yield curve extrapolation after the necking point uses a single cubic Hermite spline as before. More number of such splines after the necking point enables to achieve a complex shaped yield curve. With such a yield curve, the author believes that it is possible to obtain a better match between curves. Also, with the meshfree methods and adaptive meshes for simulation gaining popularity, one must also look into possibilities of implementing it to deal with large deformations.